

Strain Effects on Oxygen Migration in Perovskites – SUPPORTING INFORMATION

Tam Mayeshiba

Materials Science Program

University of Wisconsin-Madison, Madison, WI, 53706, USA

Dane Morgan (Corresponding Author)

Department of Materials Science and Engineering,

University of Wisconsin-Madison, Madison, WI, 53706, USA

ddmorgan@wisc.edu

Contents

| | |
|---|----|
| S1. Strain Notations..... | 3 |
| S2. 2x2x2 Supercell..... | 4 |
| S3. Orthorhombic-to-Cubic Assumption: | 4 |
| S4. Pseudopotentials, Electron Smearing, and Climbing Nudged Elastic Band (CNEB) Calculations: | 5 |
| S5. GGA vs. GGA+U..... | 6 |
| S6. Ferromagnetic, High-Spin Starting Configuration..... | 7 |
| S7. Charge Compensation: Electron-Removal Compensation versus Doping: | 9 |
| S8. Jump Directions | 12 |
| S9. Migration Barrier E_{mig} and Relationship to Ionic Conductivity:..... | 14 |
| S9a. Relating H_{mig} at Constant Pressure and E_{mig} at Constant Volume, for Unstrained and Strained Cases | 19 |
| S9b. Approximating the Defected Volume with the Undefected Volume..... | 24 |
| S10. Straining Supercells | 25 |
| S11. Fitting and Error Analysis..... | 27 |
| S12. Elastic Strain Model..... | 30 |
| S12a. Finding ν for Use in the Elastic Model | 31 |
| S12b. Finding the Bulk Modulus (for Y and V_{mig})..... | 35 |
| S12c. Finding Y for Use in the Elastic Strain Model..... | 38 |
| S12d. Finding Migration Molume for Use in the Elastic Strain Model:..... | 38 |
| Tables | 41 |
| Table S3.1. Supercell energy comparison for orthogonal versus non-orthogonal lattice vector c | 41 |
| Table S5.1. U-values for GGA+U..... | 41 |
| Table S6.1. Magnetic moment per B-site cation from FM configuration..... | 42 |
| Table S6.2. Effect of AFM structure on LaXO3 calculations..... | 43 |
| Table S6.3. Literature values for comparison with LaXO3 barriers. | 44 |
| Table S7.1. Difference between electron-removal compensated migration barriers and doped migration barriers..... | 44 |
| Table S7.2 In-plane and out-of-plane slopes for La _{0.75} Sr _{0.25} BO ₃ supercells, compared with undoped slopes..... | 45 |
| Table S8.1. Out-of-plane slopes and slope error | 45 |
| Table S8.2. Eight migration barriers in LaXO3 for several B-site cations. | 45 |
| Table S12.1. Comparing PV_{mig} for constant pressure and E_{mig} for constant volume..... | 46 |
| Table S12.2. Strained-bulk calculated Poisson's ratio, Young's modulus, and prefeactor, with errors. | 47 |
| Table S12.3. Bulk modulus values and errors..... | 47 |
| Table S12.4. Vacancy effects on bulk modulus and elastic model | 48 |
| Table S12.5. Migration volumes, calculated with BM equation or allowing volume-only relaxation..... | 48 |
| Figures..... | 49 |
| Figure S2.1. Numbered atomic positions. | 49 |
| Figure S5.1. GGA versus GGA+U no-strain migration barriers..... | 50 |
| Figure S6.1. Literature compared with LaXO3 barriers. | 51 |
| Figure S7.1 LaScO ₃ and La _{0.75} Sr _{0.25} ScO ₃ migration barrier versus strain, in-plane hop..... | 52 |

| | |
|---|----|
| Figure S7.2 LaScO ₃ and La _{0.75} Sr _{0.25} ScO ₃ migration barrier versus strain, out-of-plane hop | 53 |
| Figure S7.3 LaCrO ₃ and La _{0.75} Sr _{0.25} CrO ₃ migration barrier versus strain, in-plane hop..... | 54 |
| Figure S7.4 LaCrO ₃ and La _{0.75} Sr _{0.25} CrO ₃ migration barrier versus strain, out-of-plane hop..... | 55 |
| Figure S7.5 LaMnO ₃ and La _{0.75} Sr _{0.25} MnO ₃ migration barrier versus strain, in-plane hop | 56 |
| Figure S7.6 LaMnO ₃ and La _{0.75} Sr _{0.25} MnO ₃ migration barrier versus strain, out-of-plane hop..... | 57 |
| Figure S8.1. Migration barrier versus strain, out-of-plane hop..... | 58 |
| Figure S8.2. Migration barrier versus strain slopes for in-plane and out-of-plane hops..... | 59 |
| Figure S8.3. LaCrO ₃ barriers, all hops. | 60 |
| Figure S8.4. LaMnO ₃ barriers, all hops..... | 62 |
| Figure S8.5. Migration barrier versus strain for LaCrO ₃ , central cation position 10. | 63 |
| Figure S8.6. Migration barrier versus strain for LaMnO ₃ , central cation position 9..... | 64 |
| Figure S8.7. Slopes in migration barrier for LaCrO ₃ , all hops..... | 65 |
| Figure S8.8. Slopes in migration barrier for LaMnO ₃ , all hops. | 66 |
| Figure S8.9. Elastic strain model slopes versus slopes fit to DFT barriers, all LaCrO ₃ and LaMnO ₃ hops represented | 67 |
| Figure S10.1. Example of cubic fitting for lattice vector c fractional multiplier. | 68 |
| Figure S10.2. Fine-gridding for B=Cr..... | 68 |
| Figure S12.1. Sample V(P) curve showing a cubic fit..... | 69 |
| Figure S12.2. Vacancy effects on elastic model (compare with Figure 4 in main paper). | 70 |
| Figure S12.3. Using elastic model to try to predict V _{mig} (BM)..... | 71 |
| Figure S12.4. Using elastic model to try to predict V _{mig} (volume-only relaxation) | 72 |
| Figure S12.5. Using elastic model to try to predict slopes, with V _{mig} from volume-only relaxation | 73 |
| References | 74 |

S1. Strain Notations

Positive strain is taken as tensile strain. Negative strain is taken as compressive strain.

Strain may be given in percentages or equivalently in multipliers, e.g. +2% strain is the same as a fractional multiplier of 1.02, and -2% strain is the same as a fractional multiplier of 0.98. For some raw data uploaded with the Supporting Information, strain is given in fractional multipliers multiplied by 1000, in order to allow for fine strain gridding without using periods in directory names, e.g. 1020 indicates +2% strain, 980 indicates -2% strain, and 1002 indicates +0.2% strain, or a multiplier of 1.002.

S2. 2x2x2 Supercell

The general configuration of atoms for the 2x2x2 supercell is given in Figure S2.1, which was rendered using VESTA.¹ Atomic radii rather than crystal radii are used in this and other figures in order to prevent the cations from being obscured by the larger anions. The A-site cations are in green, numbers 1 through 8, the B-site cations are in purple, numbers 9 through 16, and the oxygen anions are in red, numbers 17 through 40. Additional oxygen atoms from neighboring repeated supercells are shown to complete the octahedra. The positions shown in Figure S2.1 are from LaMnO₃ and vary among the different compositions, although the qualitative structures are the same.

S3. Orthorhombic-to-Cubic Assumption:

The relaxed perfect supercells for the various perovskites were orthorhombic rather than perfectly cubic, with an average angle between any two lattice vectors of 90.1°, a standard deviation of 0.3°, and a range between 89.8° and 91.4°.

For all strains, we strain the perfect supercell along lattice vectors a and b and fit for the lowest-energy strain along lattice vector c (see Section S10). For each strain case in lattice vectors a and b , the fitting equation is a cubic equation of supercell energy as a function of strain along lattice vector c (details are in Section S10). The local minimum in energy of the fit function is located, and the corresponding value of the strain along lattice vector c is taken.

Adjusting lattice vector c to be orthogonal to lattice vectors a and b changes supercell energies by less than one-tenth of 1 meV, as shown in Table S3.1. Due to the small difference in supercell energies, and the simplicity of using orthogonal principal axes, in all subsequent

mathematical treatments, we assume that strain percentages along lattice vectors a , b , and c are equivalent to strain percentages along the three principal orthogonal axes, x , y , and z .

S4. Pseudopotentials, Electron Smearing, and Climbing Nudged Elastic Band (CNEB) Calculations:

The choice of PAW-GGA PW-91 pseudopotentials was based on a recommendation on the VASP website for oxides² and from previous work on perovskites.³ The soft oxygen pseudopotential was used, having a comparable maximum cutoff energy to most of the transition metal pseudopotentials, and having been shown to be adequate for many oxides.³ The cutoff energy for relaxations and static calculations was taken as 1.5 multiplied by the cutoff energy suggested for the highest cutoff energy pseudopotential in the structure.

Gaussian smearing was used for all relaxations because the structure of most of the compounds appeared semi-metallic in VASP and Gaussian smearing would produce “reasonable results in most cases,”⁴ without being prohibited for either insulators or metals. A smearing width of 0.05 eV was used for all calculations. A conjugate gradient algorithm was used for the ionic relaxations of the bulk cells and endpoints. A quasi-Newton algorithm with a force scaling factor of 0.5 was used for the nudged elastic band calculations.

The migration energy for an oxygen vacancy was determined using the climbing nudged elastic band method (CNEB) with 3 images (excluding the endpoints).^{5,6} Three images were used to ensure that the migration profile was demonstrating a single maximum rather than a local maximum-local minimum-local maximum, or to determine a more accurate energy for the global maximum. The climbing NEB method as opposed to the regular NEB method was used to ensure that one of the images climbed to the maximum energy transition state.⁵ A spring constant of -5 eV/\AA^2 was used.

In order to accomplish the NEB calculations in a quick, automated manner, a set of Python⁷ scripts was written which took in a set of parameters, such as those necessary for the INCAR and POSCAR files in VASP, and then automate the calculation process. The scripts set up and run the first calculation, wait for the calculation to complete, modify the INCAR files as necessary, and submit the next calculation in the set, until all steps in the workflow are completed. These tools are part of the MAterials Simulation Toolbox (MAST), which is under development at the University of Wisconsin-Madison.⁸

The calculation steps for no strain were as follows: 1) bulk relaxation to an energy convergence of 1 meV/atom between relaxations, 2) creation and internal relaxation of two endpoints from the bulk, 3) static calculations of both endpoints, with tetrahedral smearing with Blöchl corrections⁹ for a more accurate energy calculation, although keeping the same non-Gamma kpoint mesh, 4) linear interpolation of three images with center of mass adjustment from endpoint static runs, and using static endpoints as the NEB endpoints, 5) CNEB calculation, 6) static recalculation of all images with tetrahedral smearing. The NEB images were found to have no symmetry detected by VASP so are not expected to have any problems with trapping in high-symmetry states.

S5. GGA vs. GGA+U

Many researchers use DFT+U¹⁰ methods to treat correlations in transition metal oxides, including perovskites.³ Although many exceptions in the literature exist,^{11, 12} transition metal oxides are often treated with DFT+U in order to compensate for the electron self-interaction and excessive delocalization of d-orbital electrons in the plain GGA. Adopting values of U that have

been optimized by studying non-perovskites¹³ is often reasonable for studying related properties in an individual perovskite.

However, this study does not attempt to use U corrections due to uncertainty in their values, frequent convergence problems with their use,¹⁴⁻¹⁶ and the fact that the present work is not focused on redox energies where U seems to play a particularly important role.¹⁷ In particular, we expect that many of the errors associated with not using U will cancel when considering activation energies.

Figure S5.1 shows calculated GGA and GGA+U barriers, with some cases showing up to 1 eV difference, using U-values given in Table S5.1 (B=Sc and B=Ga are omitted as they were expected to have no need for U correction as they have no *d* valence electrons in the 3+ state). These results suggest that the overall barrier magnitude is dependent on U value. However, in general we find no correlation of strain effects with barrier magnitude (see Section S8), so the changes in barriers with U do not necessarily suggest significant changes in the strain effects. Furthermore, it is reasonable to expect that significant cancellations between barriers at different strain states will remove most of this U dependence. Therefore, we expect that our finding of decreased migration barrier with increasing tensile strain also applies to GGA+U barriers. That said, further study with U corrections and hybrid methods are clearly warranted in the future.

S6. Ferromagnetic, High-Spin Starting Configuration

Some of the LaXO₃ perovskites have antiferromagnetic (AFM) structures below a certain Néel temperature.¹⁸ The AFM structures arise from superexchange effects, mediated by the oxygen between two B-site cations.¹⁹ The A-site cations and the oxygen anions have no magnetic moment and therefore no magnetic structuring.

There was noticeable disagreement between experimentally reported magnetic moments and our calculated bulk magnetic moments for Ti, V, Fe, Co, and Ni (see Table S6.1). This discrepancy may be due to several factors, including:

- Antiferromagnetic structures in experiment not present in the calculations, which are all ferromagnetic (FM)
- Incomplete treatment of the orbital moments, as in LaTiO_3 ,²⁰ which might require the addition of the spin-orbit coupling parameter in VASP
- Excessive delocalization of d-orbital electrons, which could be at least partially corrected by using GGA+U

The magnetic moments changed noticeably between the bulk and the endpoints for B-site cations Ti, Fe, Co, and Ni, and between the endpoints and the middle NEB image (the highest energy image) for Sc, Ti, Cr, Mn, Co, and Ni. This apparent change in magnetic moment occurs whether the moment is fixed using the MAGMOM tag in the INCAR or not.

In general we model our systems as FM. This choice is motivated by the fact that for SOFCs, which is our primary motivation, these systems are used under conditions of high temperature, where they are paramagnetic. While paramagnetic order is generally not practical to model, its more metallic character is often better approximated by a ferromagnetic than AFM arrangement.³ Nonetheless, we made an attempt to consider the effect of using the experimental AFM structures in place of the FM structure on the migration barriers (see Table S6.2). This result suggests that below temperatures where magnetic ordering occurs significant alterations in barriers from our FM values are possible. However, the impact does not seem to be large enough to change a very high barrier (over 1.5 eV) to a low barrier (less than 0.5 eV) material, or vice versa.

The initial magnetic moment on an atom is set as $1\mu\text{Bohr}$ for each A-site cation, $5\mu\text{B}$ for each B-site cation, and $1\mu\text{B}$ for each oxygen anion, in a ferromagnetic configuration. We observe that VASP is able to relax these high spins to high-spin (B=Mn), intermediate-spin, low-spin, and no/nearly no magnetization states (La, O, B=Sc, B=Ga) in a sensible way, so that the A= $1\mu\text{B}$, B= $5\mu\text{B}$, O= $1\mu\text{B}$ starting configuration may be consistently applied across all systems.

Figure S6.1, with references in Table S6.3, shows that calculated migration barriers in the compensated case agree well with the results of high-temperature experiments. (More information on compensation is in Section S7). The compensated case should be more similar to the experimental doped systems than the uncompensated case. These results suggest that our ferromagnetic approximation is reasonable for treating the paramagnetic systems. More care should be taken when interpreting this data for use at lower temperature where strong magnetic ordering occurs.

S7. Charge Compensation: Electron-Removal Compensation versus Doping:

In this section, we describe our approach to compensating the charges associated with an oxygen vacancy formation and evaluate the difference between our electron-removal compensation mechanism, where we remove one oxygen atom along with two electrons, and actually doping the supercell.

An oxygen vacancy in a perovskite means that there is one fewer oxygen atom that can receive electrons donated by the cations. In order to preserve the charge neutrality of the overall crystal, the cations in the crystal must give up two fewer electrons for every oxygen vacancy, or

equivalently, one can think of the oxygen vacancy as donating two electrons to the system. The donated electrons typically reduce transition metal B site cations in the material, or are at least formally considered to do so. For pure $A^{3+}B^{3+}O_3$ perovskite, the excess electrons will generally reduce the B-site cations (which typically contain transition metals) from 3+ to 2+. However, most perovskite systems used for fast oxygen conduction have lower-valence dopant atoms on the A- or B-sites, such as Sr^{2+} , which create B^{4+} cations. For these doped systems the donated electrons may reduce some B-site cations from 4+ to 3+. In general the doping oxidizes the system more than the oxygen vacancies reduce the system, although this may not hold for all systems and can depend on temperature and oxygen partial pressure. Therefore, the system is predominantly a 4+ and 3+ B-site cation mixture and most oxygen will diffuse in an environment of 4+ and 3+ cations. The exact environment around the diffusing oxygen could be extremely complex. However, it is likely from simple electrostatic arguments that the 3+ will be closer to the vacancy and most systems are predominantly 3+. Furthermore, since doping levels and species vary, they open up a very wide-range of possible local environments. To keep the calculations tractable and avoid complexities of dopants couplings we therefore generally work with cells without explicit dopants. Thus we perform all calculations for undoped systems and 3+ cations.

In order to maintain 3+ cations even in the presence of the extra electrons donated by the oxygen vacancy we create a vacancy by removing from the supercell both an oxygen atom with its six valence electrons and an additional two electrons. This procedure is the computational equivalent of substituting lower-valence dopant atoms on A-sites or B-sites somewhere else in the crystal beyond the boundaries of the supercell. The advantage of this method is that it avoids

the interaction between oppositely-charged defects by creating a single oxygen vacancy in the supercell without using dopant atoms.

Although the avoidance of explicitly including dopants greatly simplifies the calculation, it is important to assess if this approximately approach causes significant errors in the results. We therefore also performed a series of migration energy calculations with explicit Strontium doping in order to assess if the values are similar to those of the compensated method. For the doped supercells, we remove an oxygen atom (the atom only, without removing any extra electrons) and also substitute two Strontium atoms at two of the Lanthanum A-sites. VASP relaxes these cations to a +2 and a +3 state, respectively. For the $\text{La}_{0.75}\text{Sr}_{0.25}\text{BO}_3$ series, cation positions 7 and 8 were chosen (see Figure S2.1). This positioning is arbitrary. Differences created by different positioning of the A-site defects are expected to be small compared to the margin of error associated with the overall effects of including vs. excluding dopants and other errors in due to finite size and inherent DFT limitations. For example, the migration barrier for the O29 to O30 hop in $\text{La}_{0.75}\text{Sr}_{0.25}\text{MnO}_3$ with Strontium atoms in positions 4 and 5 is 0.98 eV, while the migration barrier with Strontium atoms in positions 7 and 8 is 1.00 eV.

The migration barrier difference between the two methods of compensation is shown in Table S7.1 as the LaBO_3 electron-removal compensated barrier minus the $\text{La}_{0.75}\text{Sr}_{0.25}\text{BO}_3$ Sr-doped barrier for each B-site cation. The magnitude of the difference is on average 140 meV, with a standard deviation around this difference of +/- 69 meV. This range of differences is below the range assumed solely for jump directions (see Section S8), and is likely a result of the different geometry imposed by adding Sr atoms to the doped cell. However, the shift has a clear direction, and the effect of Sr can be more usefully thought of as raising the no-dopant simulation results by about 140 ± 69 meV. This value provides a relatively easy shift one can

apply to relate the values from the two approaches if needed. Given that the shift is relatively constant we expect that the strain response from our compensated calculations and the explicit Sr doped calculations will be similar, yielding similar energy/% strain slopes.

Overall, as this Sr coupling is hard to model accurately, electron removal is chosen to perform the strained, compensated calculations. We believe this approach better represents the pure compensation effect independent of which dopants and dopant placements are used to perform the compensation. We also believe that omitting the dopant atoms gives a more universal picture of strain effects for a given B-site cation. Nevertheless, measuring the strain effects on a variety of explicitly doped supercells would be a valuable future addition to the complete dataset. In Table S7.2 and Figure S7.1 through Figure S7.6, we provide migration barrier data for strained supercells with three explicit Sr A-site doping configurations for B-site cations Sc, Cr, and Mn. Table S7.2 shows that, with the exception of in-plane hops for Mn, the slopes for the explicitly doped supercells fall within the ± 25 meV/% strain range of slopes that we expect given all hops in a supercell (see Section S8). The difference in slopes for the in-plane doped Mn supercells, as well as their higher-than-average errors in fitting, can be attributed to the migration barrier values for compressive strained supercells which are higher than would be expected for an approximately linear trend. The underlying cause of these increased barriers requires further investigation. In any case, Table S7.2 and Figure S7.1 through Figure S7.6 show clearly that in both explicitly doped supercells and in electron-removal charge-compensated undoped supercells, oxygen migration barriers decrease with increasing tensile strain.

S8. Jump Directions

The migration of two oxygen atoms in two particular directions are calculated for each of the systems. The two calculated migration barriers were chosen so that one hop is in-plane (O31

to O30; see Figure S2.1 for positions) and one hop is out-of-plane (O29 to O30). This choice is an approximation as there are in fact multiple symmetry-independent hops in the unit cell due to the non-cubic symmetry of the low-temperature perovskite phase and the symmetry breaking of the vacancy. The in-plane hop is described in the main text, while the out-of-plane hop is plotted in Figure S8.1, with fitted slope values in Table S8.1. The slope values for the selected consistent in-plane and out-of-plane hops are plotted together in Figure S8.2. This data suggests perhaps a slight trend for more negative slopes for out-of-plane hops but this effect is almost certainly just an artifact of the specific hops and systems chosen as different hops can have quite a wide spread of slopes (see discussion below in this section). Figure S8.2 also shows that there is no clear trend in the slopes with the atomic number of the B-site cation.

The total range of barriers for systems where we have calculated all of the symmetry distinct hops is less than 300 meV (Figure S8.3 and Figure S8.4). Table S8.2 shows additional data for eight hops in different systems, with a maximum range of 600 meV and an average range of 280 +/- 160 meV. However, each particular barrier from Figure S8.3 and Figure S8.4 follows the same qualitative trend of decreasing with tensile strain that is seen for the barrier in the main text and the selected out-of-plane barrier, with representative examples given in Figure S8.5 and Figure S8.6. The range of the slopes of migration barriers for symmetry distinct hops in meV/% strain is some 50 to 70 meV/% strain from Figure S8.7 and Figure S8.8. While this range is large, all slopes for all barriers are decreasing slopes (we omit a single LaCrO₃ barrier for octahedron 9, -2% strain which had an unusual and probably erroneous total magnetic moment). We also note that the value of the slope does not correspond to the magnitude of the zero-strain barrier, and neither out-of-plane nor in-plane slopes are consistently larger than the other. Furthermore, the range in slopes does not change the overall prediction pattern for elastic theory-

based slope versus DFT-calculated slope (Figure 4 in the main text, compared with Figure S8.9). In fact, it is interesting to see that the different hops for a given B cation (Mn or Cr) have very similar slopes predicted from the simple strain model, which implies they have very similar migration volumes. However, as noted above, these different hops have quite different slopes with strain predicted by DFT.

Figure S8.3, Figure S8.4, Figure S8.7, and Figure S8.8 show that groups of similar barrier and slope patterns (central B-site cations 10, 12, 13, and 15 versus central B-site cations 9, 11, 14, and 16) correspond to groups of octahedra which are similarly tilted around the b-axis (although not identically tilted in all respects), as can be seen from Figure S2.1.

S9. Migration Barrier E_{mig} and Relationship to Ionic Conductivity:

In this paper we focus on migration energies, E_{mig} , but often wish to relate the to measured conductivities, particularly ionic conductivities. The connection between these quantities is discussed here.

Ionic conduction in perovskites is dominated by the movement of oxygen anions,^{21,22} while electronic conduction comes either from B-site cation electrons,²³ or from hole conduction at high oxygen partial pressures.²² Significant effort is made to dope the perovskite A- and B-sites in order to produce the desired amounts of electronic and ionic conduction. For example, the doping of 2+ A-site cations (call them species M) in the place of 3+ A-site cations produces 2+-charged oxygen vacancies, as shown in Equation S9.1 and Equation S9.2:²⁴

| | |
|---|--------|
| $A_2O_3 + B_2O_3 = 2ABO_3$ | (S9.1) |
| $2MO(A_2O_3) = 2M'_A + V_0^{\cdot\cdot} + 2O_0^x$ | (S9.2) |

Assuming that oxygen ions are the only mobile ionic species in the material, conductivity is given by Equation S9.3:²¹

| | |
|--|--------|
| $\sigma_{total} = \sigma_{electronic} + \sigma_{oxygen\ ions}$ | (S9.3) |
|--|--------|

The assumption that oxygen ions are the only diffusing ions is reasonable for the perovskite system, especially in the context of the major intended uses. For example, SOFC operation depends on the adsorption and separation of gaseous oxygen, its motion as oxygen anions through the device, and the eventual recombination of those oxygen anions with hydrogen on the fuel side into water. In contrast, cations do not enjoy a large concentration of cation vacancies tailored by doping (cation doping produces anion vacancies), nor do they have a similar chemical reaction pathway that encourages unidirectional motion and keeps a supply of cations available. Furthermore, cation migration barriers are typically ~2.5-3 eV, making them far less mobile than oxygen.^{25, 26} Massive cation motion may also imply phase segregation or material failure in the context of SOFCs.

Looking only at ionic conductivity, the ionic conductivity may be described through Equation S9.4, where η or C is the concentration of each species of charge-carrying ion, q is the charge on each ion, and μ is the mobility of each ion; assuming only the motion of oxygen ions, the summation only contains one term:²⁷

| | |
|--|--------|
| $\sigma_{ionic} = \sum_i \eta_i q_i \mu_i = C_i q_i \mu_i$ | (S9.4) |
|--|--------|

The Nernst-Einstein equation relates mobility to the diffusion coefficient D and changes the conductivity expression to Equation S9.5, where k is the Boltzmann constant and T is temperature, and the subscript O is used for oxygen anions, O^{2-} :²³

| | |
|--|--------|
| $\sigma_{ionic} = C_i q_i \mu_i = \frac{C_i q_i^2 D_i}{kT} = \frac{C_o q_o^2 D_o}{kT}$ | (S9.5) |
|--|--------|

When an oxygen ion moves, it swaps spots with an oxygen vacancy. The diffusion coefficient for oxygen ions, D_o , can be related to the diffusion coefficient for oxygen vacancies, D_v , through their relative concentrations C in Equation S9.6:²⁸

| | |
|-----------------------------|--------|
| $D_o = D_v \frac{C_v}{C_o}$ | (S9.6) |
|-----------------------------|--------|

Substituting in the expression for D_o and recognizing that the square of the 2- charge on an oxygen anion is equivalent to the square of the 2+ charge on an oxygen vacancy, or $q_o^2 = q_v^2$, gives Equation S9.7,

| | |
|--|--------|
| $\sigma_{ionic} = \frac{C_o q_o^2 D_o}{kT} = \frac{C_o q_o^2 D_v C_v}{kT C_o} = \frac{C_v q_o^2 D_v}{kT} = \frac{C_v q_v^2 D_v}{kT}$ | (S9.7) |
|--|--------|

or, alternatively, Equation S9.8,

| | |
|---|--------|
| $\sigma_{ionic} = C_v q_v \mu_v = \frac{C_v q_v^2 D_v}{kT}$ | (S9.8) |
|---|--------|

Vacancy concentration and vacancy diffusion are both thermally-activated and may often be at least approximately expressed as functions of temperature in Equation S9.9, Equation S9.10, and Equation S9.11, where γ is a geometric factor, a is the jump distance, and ν_o is the vibrational frequency of the moving ion, the subscript “mig” stands for migration, and the subscript “form” stands for vacancy formation:²³

| | |
|--|---------|
| $D_v = \gamma a^2 v_0 \exp\left(\frac{-G_{mig}}{kT}\right)$ | (S9.9) |
| $D_v = \gamma a^2 v_0 \exp\left(\frac{TS_{mig}}{kT}\right) \exp\left(\frac{-H_{mig}}{kT}\right)$ | (S9.10) |
| $D_v = D_{v0} \exp\left(\frac{-H_{mig}}{kT}\right)$ | (S9.11) |

(Here we use G_{mig} , E_{mig} , etc. as the Gibbs free energy and internal energy of migration; often they are also termed ΔG_{mig} or ΔE_{mig} to signify the change in energy during migration. However, since we are treating slopes in migration energy with respect to strain, or changes in change-of-energy-during-migration, we use E_{mig} for the migration barrier energy, and ΔE_{mig} for the change in that migration barrier quantity, as with respect to strain.)

We will assume that for a perovskite doped for some practical purpose, the vacancy concentration comes primarily from aliovalent doping rather than from thermal activation, with thermal activation playing only a small part for vacancy formation energies between 2.4 and 5 eV.^{3, 29} For example, for commercial LSGM ($\text{La}_{0.80}\text{Sr}_{0.20}\text{Ga}_{0.80}\text{Mg}_{0.20}\text{O}_{3-x}$),³⁰ the nominal vacancy concentration is 1 vacancy per two Strontium substitutions, or 0.1 per formula unit. Given a calculated LaGaO_3 volume of 488 \AA^3 for 8 formula units, this is $8 \times 0.1 = 0.8$ vacancies, or a vacancy concentration C_v of $(0.8/488 \text{ \AA}^3)$. In order to obtain this vacancy concentration from a purely thermally-activated process with a relatively low H_{vf} of 3 eV, the initial vacancy concentration C_{v0} would have to be thousands of vacancies/ \AA^3 at temperatures of 1173K or lower. However, for some systems the vacancy concentration will be dominated by thermally generated vacancies and the strain response of the diffusion and ionic conductivity may be strongly influenced by changes in H_{form} with strain. We do not include these effects in the present work but they are an important area for further study.

Substituting in the temperature-dependent expression for D_v in Equation S9.11 to the formula for ionic conductivity in Equation S9.8 gives Equation S9.12:

| | |
|---|---------|
| $\sigma_{ionic} = \frac{q_v^2}{kT} C_v D_{v0} \exp\left(\frac{-H_{mig}}{kT}\right)$ | (S9.12) |
|---|---------|

Across two strains at a given temperature, the ionic conductivities may be compared as in Equation S9.13. Assuming that C_v at strain 1 is similar to C_v at strain 2, we arrive at Equation S9.14:

| | |
|--|---------|
| $\frac{\sigma_{ionic,\epsilon1}}{\sigma_{ionic,\epsilon2}} = \frac{\frac{q_v^2}{kT} C_{v,\epsilon1}}{\frac{q_v^2}{kT} C_{v,\epsilon2}} \times \frac{D_{v0,\epsilon1} \exp\left(\frac{-H_{mig,\epsilon1}}{kT}\right)}{D_{v0,\epsilon2} \exp\left(\frac{-H_{mig,\epsilon2}}{kT}\right)}$ | (S9.13) |
| $\frac{\sigma_{ionic,\epsilon1}}{\sigma_{ionic,\epsilon2}} \approx \frac{D_{v0,\epsilon1}}{D_{v0,\epsilon2}} \exp\left(\frac{-H_{mig,\epsilon1} + H_{mig,\epsilon2}}{kT}\right)$ | (S9.14) |

We recognize that D_{v0} has contributions from geometric factors, a correlation term, and phonons. Phonons are likely to be only weakly dependent on strain,³¹ the correlation term is constant for dilute vacancies, and the overall geometric factors for the cell should be similar for small strains. These assumptions yield Equation S9.15, giving the ratio of ionic conductivities at different strains. The assumption that C_v is independent of strain is likely not true in general, and Equation S9.14 and Equation S9.15 should be taken as limiting cases which include only the strain effect through migration energies without contributions from changes in vacancy content. However, we note that for doped perovskites, as are often used in oxygen conducting applications, the vacancy concentration is largely controlled by dopant concentration and not

defect formation enthalpies. Under these quite common circumstances we do expect the vacancy concentration to have only a weak dependence on strain.

| | |
|--|---------|
| $\frac{\sigma_{ionic,\epsilon1}}{\sigma_{ionic,\epsilon2}} \approx \exp\left(\frac{-H_{mig,\epsilon1} + H_{mig,\epsilon2}}{kT}\right)$ | (S9.15) |
|--|---------|

At a given temperature, making the assumption that all other quantities stay equal, Equation S9.15 makes it straightforward to relate changes in H_{mig} to changes in conductivity. To translate experimental or literature data giving trends in σ_{ionic} into a comparable slope value of $\Delta H_{mig}/\%$ strain we simply invert Equation S9.15 and divide the changes in H_{mig} by the changes in strain to produce a slope. We report and compare these slopes directly to our calculated $\Delta E_{mig}/\%$ strain slopes. We justify the equivalence of the experimental constant-pressure strained migration enthalpies H_{mig} and our calculated constant-volume strained migration barriers E_{mig} in Section S9a, Section S9b, and Section S9c below.

S9a. Relating H_{mig} at Constant Pressure and E_{mig} at Constant Volume, for Unstrained and Strained Cases

The following derivation will show that what is calculated with DFT, which is E_{mig} at constant volume per formula unit v' , is approximately equivalent to H_{mig} at constant pressure P' .

Suppose a diffusion experiment is run at some pressure P' and temperature T . Making the assumptions described in Section 9 above in order to relate conductivities, we extract out a H_{mig} at pressure P' . This pressure P' is consistent from the initial defected state through the transition state to the final defected state. The initial defected state has a volume of v' per formula unit, or a total volume of $V_{ol}=Nv'=V'$, where N is the number of formula units. The transition state has a

slightly different volume (in order to stay at pressure P'), which we define as $V_{tst} = Nv' + V_{mig}(P') = V' + V_{mig}(P')$, where $V_{mig}(P')$ is the volume change associated with the atomic migration at pressure P' .

Now suppose we have a migration barrier calculation whose initial defected state is set to that same pressure P' with the characteristic per-formula-unit volume v' , or total volume Nv' , for the same number of formula units as in the experiment (although practically speaking this would not be the case). For better convergence in the CNEB calculation, we fix the volume rather than the pressure, so that the transition state remains at constant volume Nv' , but its pressure increases.

We define two internal energies as functions of different variables: internal energy E as a function of volume V , and internal energy U as function of pressure P . Note that here U is not the finite temperature internal energy, but still the zero-temperature internal energy equivalent to E but written as a function of pressure. Then we define the migration energy as the transition state energy, E_{tst} or U_{tst} , minus the energy of the initial defected state when the oxygen (or vacancy) is on the lattice site, E_{ol} or U_{ol} , in Equation S9a.1 and Equation S9a.2. Note that because we are in a finite size supercell which can impact our results we explicitly keep N as an independent variable.

The transition state energy can be split into a bulk-like term and a term associated with the transitioning atom (here, a single oxygen) and its surrounding atomic relaxations. The bulk-like term is an energy component that scales linearly with the number of formula units N . The term associated with the transitioning atom and its surrounding atomic relaxations, on the other hand, does not depend on the number of formula units N for large N . For very few formula units, this local energy term may be affected by the supercell size, but as the calculation supercell gets

larger, the local energy term converges to an asymptotic value. This dependence yields S9a.3 for all N , and S9a.4 for N large enough that E_l has reached its asymptotic value. We note that ε_0 is just the energy per formula unit of the host system, here the undefected perovskite.

| | |
|--|---------|
| $E_{mig}(V, N) = E_{tst}(V, N) - E_{ol}(V, N)$ | (S9a.1) |
| $U_{mig}(P, N) = U_{tst}(P, N) - U_{ol}(P, N)$ | (S9a.2) |
| $E_{tst}(V, N) = N\varepsilon_0(v) + E_1(V, N)$ | (S9a.3) |
| $E_{tst}(v, N) = N\varepsilon_0(v) + E_1(v)$ (<i>in large N limit</i>) | (S9a.4) |

As we will from here forward be considering only cases where N is large enough that Equation S9a.4 holds and is otherwise fixed, we will not explicitly write the dependence on N in the following equations except when it is needed for clarity. Using the definition of enthalpy, $H_{mig}(P')$ can be written as Equation S9a.5 Using the definition of migration energy, $H_{mig}(P')$ can be further split into Equation S9a.6.

Now we make two major substitutions, changing the energy definition in the enthalpy from an energy U as a function of pressure P to an energy E as function of volume V . First, for the on-lattice energy, the on-lattice pressure P' was defined as having a corresponding volume V' , so we substitute the energy $E_{ol}(V')$ for the energy $U_{ol}(P')$ (*since they are the same value*), giving Equation S9a.7. Second, for the transition-state energy, the transition state pressure P' was defined as having corresponding transition state volume $V_{tst} = V' + V_{mig}(P')$. Therefore, we substitute the energy $E_{tst}(V' + V_{mig}(P'))$ for the energy $U_{tst}(P')$, to give Equation S9a.8.

| | |
|--|---------|
| $H_{mig}(P') = U_{mig}(P') + P'V_{mig}(P')$ | (S9a.5) |
| $H_{mig}(P') = U_{tst}(P') - U_{ol}(P') + P'V_{mig}(P')$ | (S9a.6) |

| | |
|--|---------|
| $H_{mig}(P') = U_{tst}(P') - E_{ol}(V') + P'V_{mig}(P')$ | (S9a.7) |
| $H_{mig}(P') = E_{tst}(V' + V_{mig}(P')) - E_{ol}(V') + P'V_{mig}(P')$ | (S9a.8) |

In Equation S9a.9, we Taylor expand the E_{tst} term.

| | |
|---|---------|
| $E_{tst}(V' + V_{mig}(P'))$ | (S9a.9) |
| $= E_{tst}(V') + V_{mig}(P') \frac{dE_{tst}(V)}{dV} \Big _{V'} + \frac{1}{2!} (V_{mig}(P'))^2 \frac{d^2 E_{tst}(V)}{dV^2} \Big _{V'}$ | |
| $+ \dots$ | |

Using the implication of Equation S9a.4 that E_{tst} is a function of only N and v , and noting that at fixed N , $\frac{d}{dV} = \frac{1}{N} \frac{d}{dv}$, Equation S9a.9 can be rewritten as Equation S9a.10.

| | |
|---|----------|
| $E_{tst}\left(\frac{V' + V_{mig}(P')}{N}, N\right)$ | (S9a.10) |
| $= E_{tst}(v', N) + V_{mig}(P') \frac{dE_{tst}(v', N)}{Nd v'} \Big _{v'}$ | |
| $+ \frac{1}{2!} (V_{mig}(P'))^2 \frac{d^2 E_{tst}(v', N)}{N^2 d v'^2} \Big _{v'} + \dots$ | |

Now substituting in Equation S9a.4 for E_{tst} and dropping terms of $O(1/N)$ and higher powers of $1/N$ gives Equation S9a.11.

| | |
|---|----------|
| $E_{tst}\left(\frac{V' + V_{mig}(P')}{N}, N\right) = E_{tst}(v', N) + V_{mig}(P') \frac{d\varepsilon_0(v')}{d v'} \Big _{v'}$ | (S9a.11) |
|---|----------|

| | |
|------------------------------------|--|
| $= E_{tst}(v', N) - P'V_{mig}(P')$ | |
|------------------------------------|--|

Here we have defined used the fact that, as ε_0 is the bulk system energy per formula unit, its volume per formula unit derivative is just the negative pressure. Equation S9a.11 can be rewritten in terms of our total volumes as Equation S9a.12.

| | |
|---|----------|
| $E_{tst}(V' + V_{mig}(P')) = E_{tst}(V') - P'V_{mig}(P')$ | (S9a.12) |
|---|----------|

Substituting Equation S9a.12 into Equation S9a.8 yields Equation S9a.13, Equation S9a.14, and Equation S9a.15..

| | |
|--|----------|
| $H_{mig}(P') = E_{tst}(V') - P'V_{mig}(P') - E_{ol}(V') + P'V_{mig}(P')$ | (S9a.13) |
| $H_{mig}(P') = E_{tst}(v', N) - E_{ol}(V')$ | (S9a.14) |
| $H_{mig}(P') = E_{mig}(V')$ | (S9a.15) |

We reiterate that the above only holds for large enough N that we can use Equation S9a.4 and drop terms of $O(1/N)$ in the Taylor expansion in Equation S9a.10. With this result, we see that constant-volume migration barrier energies for a large enough supercell size can be used to approximate the values for constant-pressure enthalpies, assuming low temperature.

Note that the above derivation directly applies only for an isotropic system. However, in the general case one may have a migrating atom with an isotropic migration volume tensor and under mixed boundary coundiation, with some components at fixed strain and others at fixed stress. One can again ask the question whether the correct migration free energy (at low temperature) under the mixed boundary conditions is well represented by a fixed volume (and with fixed lattice vectors) ab inito calculated energy difference. The above derivation readily

generalizes to this more complex situation, as each $\sigma_{ij}\epsilon_{ij}$ component of the migration energetics can be treated independently. If the migration is at fixed ϵ_{ij} then the calculation is being done at directly comparable boundary conditions. If the migration is at fixed σ_{ij} then the calculation is approximately correct through an argument parallel to that above for the specific ij component.

S9b. Approximating the Defected Volume with the Undefected Volume

In Section S9a we assumed that the starting pressure and volume for the calculations were P' and V' , respectively, which is the volume for the defected supercell. However, the starting volume in our calculations is really V_0 , the volume of the undefected supercell, or rather \bar{V}_0 with strain, where we use the bar over the variable to represent its value in our strained calculations. Therefore, the starting pressure is some \bar{P}_0 which is then modified by the effects of introducing a vacancy, and at volume \bar{V}_0 rather than \bar{V}' , the starting pressure is not exactly \bar{P}' . That said, with large enough cells (enough formula units N), these differences in volume and pressure diminish, as there is only one vacancy being introduced in a background of many formula units N , so the derivations in Section S9a still hold.

Through all of Section S9a and Section S9b we mention “large enough” formula units N . Our supercell sizes at an undefected supercell of 40 atoms or $N=8$ are not large enough for the approximations to become equalities within the limits of precision. However, we show in Table S12.1 (Section S12) that our values using migration energies are comparable with expected strain model values using isotropic pressures and volumes, even with our various assumptions,

approximations, and distinctions (e.g. in starting pressures and volumes), and even at our relatively small $N=8$.

S10. Straining Supercells

Strains along lattice vectors a and b were taken at $\pm 1\%$ and $\pm 2\%$ of the original lattice parameters, with positive values as tensile strain and negative values as compressive strain (for example, tensile strain of $+2\%$ would strain the lattice parameter to 1.02 times the original lattice parameter and a compressive strain of -2% would strain the lattice parameter to 0.98 times the original lattice parameter). Lattice mismatch strains of up to ~ 7 percent have been reported, although thin films may not allow as much strain, and strain may produce segregated phases.³²⁻³⁴

For each strain case (with lattice vectors a and b having equal fixed strains), the response in lattice parameter c , and therefore also the strained volume, was found by fitting a cubic function to the energies of a series of bulk calculations with different lattice vector c strains. At least seven lattice vector c strains were calculated to produce data points for the fit, in 1% steps in a range about 3% above and 3% below the estimated lattice vector c strain value, which from experience was known to be somewhat smaller than that given by a volume-conserving response. Each strain case consisted of a low kpoint-mesh ($2 \times 2 \times 2$ M) initial internal optimization, a $4 \times 4 \times 4$ M kpoint-mesh internal optimization, and a static calculation, all at fixed volume (once the strain had been applied) and cell shape. Additional lattice vector c points were calculated as necessary, for example, in order to distinguish between two distinct magnetic moment curves with B-cations Fe, Co, and Ni, and to choose only those points on a curve consistent with the magnetic moment trending near the volumetrically-likely lattice vector c strain (see Figure S10.1). To further explore the trends of c axis with strain, the lattice vector c strains were plotted against the lattice vector a and b strains. Fine-gridding of LaCrO_3 showed that such a plot is a

smooth curve, fitting well to a quadratic function (see Figure S10.2). The fitted minimum-energy lattice vector c strain for each biaxial strain case was subsequently used, along with the strained lattice vectors a and b , to fix the volume and cell shape in all further calculations for that strain case and chemical system. Note that 0% strain was also subjected to the same fitting treatment, and we found that in most cases, 0% strain in lattice vectors a and b did not, in fact, correspond to 0% strain in lattice vector c but rather to a magnitude of 0.3% strain or lower, indicating small convergence errors in the original groundstate calculations.

We note that the total volume of a system could vary by as much as 5% among different strain states due to different equilibrium c lattice parameter values.

Each undefected strain state bulk was allowed to relax only internally, and then the endpoint and NEB calculations proceeded as outlined in Section S2 through Section S7.

Occasionally, for systems B=V, Fe, Ni, where we were interested in checking apparent deviations from a linear slope in E_{mig} with strain, more fine-gridded strains in a and b lattice parameters were evaluated, using a lattice parameter c based on the quadratic fit of c vs. strain in a . Also, some systems' defected endpoints and NEB images were started over using the fractional coordinates of the same system at a different strain to explore for metastable solutions. In these cases, the lowest-energy activated state energy, which corresponds to the lowest-energy barrier (since the endpoints remained the same), was taken to calculate the barrier. The finely gridded B=Cr system shows that for a well-behaved system, migration barrier versus strain falls along a smooth line (see B=Cr case in Figure 1 in the main text).

Outlier points occasionally exhibited some sort of polymorphic distortion, e.g. when comparing middle images among strain cases, an O-B-O bond angle for LaVO₃ suddenly changed its sign at the zero-strain case and then back again, rather than changing gradually with

increasing tensile strain. An NEB calculation for LaVO_3 restarting with randomly perturbed images found a very close energy (within 0.005 eV per 8 formula units) defected structure with a completely different and rotated octahedron tilt configuration, although the oxygen vacancy remained in the same place. The Generalized Gradient Approximation (GGA) method used in this work (see Section S5) may also lead to unstable magnetic moments; for example, our GGA LaFeO_3 , LaNiO_3 , and LaCoO_3 systems showed different magnetic moments under different strain states (with a fluctuation of 0.35, 0.3, and 0.4 μB per Fe, Ni, and Co). Fixing magnetic moments could be arbitrary (for example, the magnetic moment for Ni in LaNiO_3 in GGA could vary between 0 and 0.4 μB per Ni across all strain cases, up to 0.3 μB per Ni within a single strain case, and up to 0.3 μB per Ni within a single NEB), and changes in magnetic moment profiles of NEBs from one strain case to another or between two NEBs of the same strain cases may also be a function of polymorphism. Total convergence among polymorphs and magnetic moments appears to be quite challenging and was not necessary to illustrate the clear overall trends we observe here, so we do not discuss them further in this paper.

S11. Fitting and Error Analysis

For linear and quadratic fits, error analysis was derived from Hocking³⁵ as follows:

Our input variables are assumed to have no error, as they are set deliberately to a certain value (e.g. epitaxial strain, or system volume). These inputs correspond to the x -vector in Hocking's treatment, column vector $[x_1; x_2; \dots; x_N]$. Our output variables, like migration barrier and pressure, correspond to the y -vector.

For a fit where the output axis intercept will be one of the fitting coefficients (e.g. there will be a +constant term at the end), we use X-matrices for linear and quadratic fits, as in Equation S11.1:

| | |
|--|---------|
| $X = [\vec{j}\vec{x}] \text{ or } [\vec{j}\vec{x}\vec{x}^2]$ | (S11.1) |
|--|---------|

where vector \mathbf{J} is a column vector of ones. In this notation $\bar{a}\bar{b}$ represents an $N \times 2$ matrix with the first column consisting of the $N \times 1$ vector \bar{a} and the second column consisting of the $N \times 1$ vector \bar{b} .

For a fit where the output axis intercept (e.g. y-intercept) is set to zero, we use the following X-matrices for linear and quadratic fits, as in Equation S11.2:

| | |
|--|---------|
| $X = [\vec{x}] \text{ or } [\vec{x}\vec{x}^2]$ | (S11.2) |
|--|---------|

The coefficient matrix β , with the lowest-order coefficient appearing as the top-most element, is found in Equation S11.3:

| | |
|--|---------|
| $\hat{\beta} = (X^T X)^{-1} X^T \vec{y}$ | (S11.3) |
|--|---------|

The “hat” matrix H is given in Equation S11.4:

| | |
|-------------------------|---------|
| $H = X(X^T X)^{-1} X^T$ | (S11.4) |
|-------------------------|---------|

The estimated standard deviation, squared, is given in Equation (S11.5):

| | |
|--|---------|
| $s^2 = \frac{\sigma^2 \chi^2(N - p)}{N - p} \approx \frac{RSS}{N - p} = \frac{RSS}{rank(I - H)}$ | (S11.5) |
|--|---------|

where I is an appropriately-sized identity matrix, N is the sample size (number of input, output pairs), and RSS is the residual sum of squares, defined below in Equation (S11.6) and Equation (S11.7) the residual r_i is the difference between the observed and estimated value of the output. Note that when using Python's numpy package, the method `numpy.linalg.matrix_rank` should be used to calculate $rank(I-H)$, rather than using `numpy.rank`.

| | |
|----------------------------|---------|
| $RSS = \sum_{i=1}^N r_i^2$ | (S11.6) |
| $r_i = y_i - \hat{y}_i$ | (S11.7) |

The variance and therefore standard error in the coefficients themselves is given in vector form in Equation (S11.8):

| | |
|---|---------|
| $var[\hat{\beta}_i] = (std\ errors^2) = diag((X^T X)^{-1}) * s^2$ | (S11.8) |
|---|---------|

Explicitly, for the DFT-fitted slopes, the standard error therefore works out to Equation S11.9, where the standard error in the slope, s_{β_1} , is given as a function of the residual sum of squares $\sum r_i^2$ and the sum of input squares, where x_i are the input percent strains (e.g. “-2”):

| | |
|--|---------|
| $s_{\hat{\beta}_1} = \sqrt{\frac{1}{N-2} \frac{\sum_{i=1}^N r_i^2}{\sum_{i=1}^N (x_i - \bar{x})^2}}$ | (S11.9) |
|--|---------|

S12. Elastic Strain Model

We make extensive comparison to the simple elastic model proposed by Schichtel et al.,³⁴ which relates strain and pressure as in Equation S12.1:

| | |
|---|---------|
| $p = -\frac{2}{3} \left(\frac{Y}{1-\nu} \right) \epsilon_{12}$ | (S12.1) |
|---|---------|

Here ϵ_{12} is biaxial strain, Y is the Young's modulus, ν is the Poisson's ratio, and p is the resulting pressure. At zero strain, the pressure is zero, so p can also be given as the change in pressure due to strain, where $\Delta p = p - 0$. Therefore, at fixed temperature and for an unchanging number of particles, a change in migration Gibbs free energy due to pressure goes as Equation S12.2 and Equation S12.3, assuming that migration volume V_{mig} changes little at different strains (an assumption which is supported by our data in Table S12.1):

| | |
|---|---------|
| $\Delta G_{mig} = V_{mig} \Delta p = -\frac{2}{3} \left(\frac{Y}{1-\nu} \right) \epsilon_{12} V_{mig}$ | (S12.2) |
| $\frac{\Delta G_{mig}}{\epsilon_{12}} = -\frac{2}{3} \left(\frac{Y}{1-\nu} \right) V_{mig}$ | (S12.3) |

Rearranging Equation S12.2 gives $\Delta G_{mig}/\Delta p = V_{mig}$, for a fixed-pressure, constant temperature system for a given strain case. As in Section S9, our calculated E_{mig} , which are done at fixed volume at each strain case, can be thought of as equivalent to G_{mig} , giving Equation S12.4 for the predicted results from the Schichtel model for our calculated slopes.

| | |
|--|---------|
| $\frac{\Delta E_{mig}}{\epsilon_{12}} = -\frac{2}{3} \left(\frac{Y}{1-\nu} \right) V_{mig}$ | (S12.4) |
|--|---------|

Table S12.1 shows, first, that the perfect strained cell pressures are similar to those expected from Equation S12.1 and, second, that were we to take a fixed strained pressure and a fit-calculated migration volume (Section S12d), we would arrive at a ΔG_{mig} value similar to that predicted by Equation S12.2 and also similar to our directly-calculated ΔE_{mig} values.

The comparison in the text shows that there are a number of quantitative discrepancies between predictions from this strain model and the migration energy slopes calculated directly with ab initio methods.

S12a. Finding ν for Use in the Elastic Model

For a linearly elastic isotropic material, the strain energy density U is given in Equation S12a.1, where the principal axes are denoted by subscripts 1, 2, and 3.³⁶

| | |
|--|----------|
| $U = \frac{1}{2}\lambda(\epsilon_1 + \epsilon_2 + \epsilon_3)^2 + G(\epsilon_1^2 + \epsilon_2^2 + \epsilon_3^2)$ | (S12a.1) |
|--|----------|

The elastic constants λ and G can be written in terms of the Poisson's ratio ν and Young's modulus Y of the material (given as E in the reference text), in Equation S12a.2 and Equation S12a.3, which may be substituted into Equation S12a.1 to give Equation S12a.4.

| | |
|---|----------|
| $\lambda = \frac{\nu Y}{(1 + \nu)(1 - 2\nu)}$ | (S12a.2) |
| $G = \frac{Y}{2(1 + \nu)}$ | (S12a.3) |
| $U = \frac{\nu Y}{2(1 + \nu)(1 - 2\nu)}(\epsilon_1 + \epsilon_2 + \epsilon_3)^2 + \frac{Y}{2(1 + \nu)}(\epsilon_1^2 + \epsilon_2^2 + \epsilon_3^2)$ | (S12a.4) |

Using $\epsilon_1 = \epsilon_2$ for biaxial strain, ϵ_3 is obtained from the lattice vector c fitting, and is not equal to zero, as the cases discussed here are for the thin-film plane stress case, rather than for a plane strain case.

The strain energy density U is the change in energy due to strain, per unit volume when strained, and was defined as in Equation S12a.5:

| | |
|--|----------|
| $U = \frac{E_{strained}^{bulk\ supercell} - E_{unstrained}^{bulk\ supercell}}{V_{strained}^{bulk\ supercell}}$ | (S12a.5) |
|--|----------|

In principle, it is possible to perform a nonlinear fit using the strain and strain energy data in order to find λ and G or Y and ν . However, in practice, such fitting produced unreasonable negative Poisson's ratios and was in general badly determined, with large ranges of constant pairs that had very similar root-mean-squared errors.

Instead, we use the plane-stress approximation to calculate a Poisson's ratio ν from our data, then use the Poisson's ratio and the bulk modulus to calculate the Young's modulus Y . From Barber, we obtain Equation S12a.6, Equation S12a.7, and Equation S12a.8 for the plane-stress case ($\sigma_{zz}=0$), where E is the Young's modulus.³⁷ Given that ϵ_{xx} and ϵ_{yy} are identical for our cells, and taking the approximation that σ_{xx} and σ_{yy} for our near-cubic cells are also equal, we derive Equation S12a.9 through Equation S12a.15.

| | |
|--|----------|
| $\epsilon_{zz} = \frac{-\nu}{E} (\sigma_{xx} + \sigma_{yy})$ | (S12a.6) |
| $\epsilon_{xx} = \frac{\sigma_{xx}}{E} - \frac{\nu\sigma_{yy}}{E}$ | (S12a.7) |
| $\epsilon_{yy} = \frac{\sigma_{yy}}{E} - \frac{\nu\sigma_{xx}}{E}$ | (S12a.8) |

| | |
|---|-----------|
| $\epsilon_{xx} = \epsilon_{yy} = \frac{\sigma_{xx}}{E} - \frac{\nu\sigma_{yy}}{E} = \frac{\sigma_{xx}}{E} - \frac{\nu\sigma_{xx}}{E}$ | (S12a.9) |
| $\epsilon_{xx} = \frac{(1 - \nu)\sigma_{xx}}{E}$ | (S12a.10) |
| $\sigma_{xx} = \frac{E\epsilon_{xx}}{(1 - \nu)}$ | (S12a.11) |
| $\epsilon_{zz} = \frac{-2\nu\sigma_{xx}}{E}$ | (S12a.12) |
| $\epsilon_{zz} = \frac{-2\nu E\epsilon_{xx}}{E(1 - \nu)}$ | (S12a.13) |
| $\frac{\epsilon_{zz}}{\epsilon_{xx}} = \frac{-2\nu}{(1 - \nu)}$ | (S12a.14) |
| $\nu = \frac{\frac{\epsilon_{zz}}{\epsilon_{xx}}}{\left(\frac{\epsilon_{zz}}{\epsilon_{xx}} - 2\right)} = \frac{\frac{\epsilon_c}{\epsilon_a}}{\left(\frac{\epsilon_c}{\epsilon_a} - 2\right)}$ | (S12a.15) |

Using the definition of engineering strain as $\Delta L/L$,³⁸ and noting that our zero-strain fractions are 1 for lattice vectors a and b , but usually slightly over 1 for lattice vector c due to fitting (explained in Section S10, Straining supercells, e.g. 1.003), we take strains from Equation S12a.16 through Equation S12a.18, where “strain fraction” is the strain fraction multiplier, e.g. 1, 1.02, 0.99, etc.)

| | |
|--|-----------|
| $\epsilon_a = \frac{(\text{strain fraction } a - 1) * a}{a} = (\text{strain fraction } a) - 1$ | (S12a.16) |
| $\epsilon_c = \frac{(\text{strain fraction } c - \text{zero strain fraction } c) * c}{c}$ | (S12a.17) |
| $\epsilon_c = \text{strain fraction } c - \text{zero strain fraction } c$ | (S12a.18) |

These normalized ϵ_c values were fit against the ϵ_a values to produce a quadratic fit, Equation S12a.19. Because zero strain in a should produce zero strain in c by definition (and from the normalization in Equation S12a.18, the intercept g in Equation S12a.19 is set as zero. Substituting Equation S12a.19 into our Equation S12a.15 for Poisson's ratio produces Equation S12a.20.

| | |
|--|-----------|
| $\epsilon_c = d\epsilon_a^2 + f\epsilon_a + g = d\epsilon_a^2 + f\epsilon_a$ | (S12a.19) |
| $v = \frac{\frac{\epsilon_c}{\epsilon_a}}{\left(\frac{\epsilon_c}{\epsilon_a} - 2\right)} = \frac{\epsilon_c}{\epsilon_c - 2\epsilon_a} = \frac{d\epsilon_a^2 + f\epsilon_a}{d\epsilon_a^2 + f\epsilon_a - 2\epsilon_a} = \frac{d\epsilon_a + f}{d\epsilon_a + (f - 2)}$ | (S12a.20) |

To take v as a material constant defined at small strains, we take v in the limit as ϵ_a goes to zero and arrive at Equation S12a.21 (remember that here, f is just the first-order coefficient of the fit of ϵ_c as a function of ϵ_a), with error defined in Equation S12a.22 and Equation S12a.23.

| | |
|--|-----------|
| $v = \frac{f}{f - 2}$ | (S12a.21) |
| $\left(\frac{\sigma_v}{v}\right) = \sqrt{\left(\frac{\sigma_f}{f}\right)^2 + \left(\frac{\sigma_f}{f}\right)^2}$ | (S12a.22) |
| $\sigma_v = v \left(\frac{\sigma_f}{f}\right) \sqrt{2}$ | (S12a.23) |

σ_f is the first element of the matrix in Equation S12a.24 and the X matrix is defined in Equation S12a.25. (There is no J -vector of ones, since the intercept is set to (0,0).)

| | |
|--|-----------|
| $\left[\text{diag}((X^T X)^{-1}) * \frac{\text{RSS of } \epsilon_c(\epsilon_a)}{\text{rank}(I - H \text{ of } \epsilon_c(\epsilon_a))} \right]$ | (S12a.24) |
|--|-----------|

| | |
|--|-----------|
| $X = \left[\overrightarrow{\epsilon}_a \overrightarrow{\epsilon}_a^2 \right]$ | (S12a.25) |
|--|-----------|

The calculated Poisson's ratio values are given in Table S12.2. It is possible that the introduction of an oxygen vacancy may change the Poisson's ratio for the 2x2x2 simulation supercells. However, this effect has not been included in the present calculations. We use the Poisson's ratio calculated from perfect cells as a materials constant and do not include effects of the vacancy.

S12b. Finding the Bulk Modulus (for Y and V_{mig})

Finding the bulk modulus was necessary for calculating the Young's modulus Y and the migration volume V_{mig} . In order to calculate the bulk modulus B_0 and the derivative of the bulk modulus, B_0' , for each system, nine pressure-volume pairs of the perfect bulk were calculated for each system. Each pressure-volume point was a static calculation at a different volume, where the volume was equally strained along each lattice vector a , b , and c , starting at 5% compressive strain and increasing in increments of 1% to 3% tensile strain. In the following fitting we found that the direct fit to a Birch-Murnaghan equation was numerically unstable and gave results very sensitive to the initial values chosen in the optimization. Therefore, we have first fit to a cubic equation and then used the results of that fit to obtain the parameters for the Birch-Murnaghan equation.

The nine points were easily fit to a well-matching cubic equation for each system, producing $V(P)$ (see Figure S12.1). The coefficients of the cubic fit were then used to derive the bulk modulus, B_0 , and its derivative, B_0' , as shown in Equation S12b.1 through Equation S12b.14:

| | |
|---|-----------|
| $B_0 = -V \left(\frac{\partial P}{\partial V} \right)_{P=0}$ | (S12b.1) |
| $B = -V \left(\frac{\partial P}{\partial V} \right)$ | (S12b.2) |
| $B = \frac{-V}{\left(\frac{\partial V}{\partial P} \right)}$ | (S12b.3) |
| $V(P) = jP^3 + kP^2 + lP + m, \{j, k, l, m\} \in \mathbb{R}$ | (S12b.4) |
| $\left(\frac{\partial V}{\partial P} \right) = 3jP^2 + 2kP + l$ | (S12b.5) |
| $B = \frac{-V}{\left(\frac{\partial V}{\partial P} \right)} = \frac{-(jP^3 + kP^2 + lP + m)}{3jP^2 + 2kP + l}$ | (S12b.6) |
| $B_0 = \frac{-V}{\left(\frac{\partial V}{\partial P} \right)_{P=0}} = \frac{-(0 + 0 + 0 + m)}{0 + 0 + l} = \frac{-m}{l}$ | (S12b.7) |
| $B_0 = \frac{-m}{l}$ | (S12b.8) |
| $\sigma_{B_0} = B_0 \sqrt{\left(\frac{\sigma_m}{m} \right)^2 + \left(\frac{\sigma_l}{l} \right)^2}$ | (S12b.9) |
| $B'_0 = \left(\frac{\partial B}{\partial P} \right)_{P=0} = \frac{\left(\frac{-\partial V}{\partial P} \right) \left(\frac{\partial V}{\partial P} \right) - \left(\frac{\partial^2 V}{\partial P^2} \right) (-V)}{\left(\frac{\partial V}{\partial P} \right) \left(\frac{\partial V}{\partial P} \right)} = -1 + \frac{V \left(\frac{\partial^2 V}{\partial P^2} \right)}{\left(\frac{\partial V}{\partial P} \right) \left(\frac{\partial V}{\partial P} \right)} \Bigg _{P=0}$ | (S12b.10) |
| $\left(\frac{\partial^2 V}{\partial P^2} \right) = 6jP + 2k$ | (S12b.11) |
| $B'_0 = -1 + \frac{(jP^3 + kP^2 + lP + m)(6jP + 2k)}{(3jP^2 + 2kP + l)(3jP^2 + 2kP + l)} \Bigg _{P=0}$ | (S12b.12) |
| $B'_0 = -1 + \frac{(0 + 0 + 0 + m)(0 + 2k)}{(0 + 0 + l)(0 + 0 + l)}$ | (S12b.13) |

| | |
|-------------------------------|-----------|
| $B'_0 = -1 + \frac{2mk}{l^2}$ | (S12b.14) |
|-------------------------------|-----------|

(Remember that k , l , and m are just real-valued coefficients.)

The error in the coefficients j , k , l , and m can be approximated as the fourth, third, second, and first elements, respectively, of the matrix in Equation S12b.15, with the X-matrix given in Equation (S12b.16). The calculated bulk moduli and their errors are given in Table S12.3.

| | |
|--|-----------|
| $\left[\text{diag}((X^T X)^{-1}) * \frac{\text{RSS of } V(P)}{\text{rank}(I - H \text{ of } V(P))} \right]$ | (S12b.15) |
| $X = \left[\vec{j} \vec{P} \vec{P}^2 \vec{P}^3 \right]$ | (S12b.16) |

Although we calculated the bulk modulus for the undefected system, it is possible that it is altered by the specific state of the system during the calculation of the migration energies. As we wish to compare the strain model to the migration energy calculations such a change in bulk modulus could produce errors. In particular, vacancy concentration (presence or absence of the single vacancy), placement (initial or activated state), and compensation status (compensated using electron removal or uncompensated) can all have an effect on bulk modulus, as given in Table S12.4. The strain data is for compensated systems, so using bulk modulus in the presence of the compensated vacancy, the two check cases (B=Cr and B=Mn) indicate an increase in the bulk modulus and therefore in the Young's modulus Y (using the Poisson's ratio from Section S12a), prefactor, and magnitude of the calculated elastic model slope. The full elastic model could be redone with all bulk modulus calculations at the same vacancy concentration, placement, and compensation status as the migration barrier calculations, rather than using the undefected-cell bulk modulus. However, Figure S12.2 shows that including the effect of the vacancy on the bulk modulus, using the largest downward shift to the elastic model slope, still leaves significant error between the elastic model slopes and the DFT-fit slopes. The main conclusion remains that the elastic model provides a good qualitative, if not quantitative, description of the change in migration barrier versus strain.

S12c. Finding Y for Use in the Elastic Strain Model

Using our bulk modulus values, we calculate the Young's modulus Y from Equation S12c.1.³⁶ The error is given in Equation S12c.2.

| | |
|---|----------|
| $Y = 3B_0(1 - 2\nu) = 3B_0 - 6B_0\nu$ | (S12c.1) |
| $\sigma_Y^2 = 3^2\sigma_{B_0}^2 + 6^2(B_0\nu)^2 \left[\left(\frac{\sigma_{B_0}}{B_0}\right)^2 + \left(\frac{\sigma_\nu}{\nu}\right)^2 \right]$ | (S12c.2) |

Therefore, our prefactor for the elastic model is defined in Equation S12c.3, with error treatment in Equation S12c.4:

| | |
|---|----------|
| $prefactor = \frac{-2Y}{3(1 - \nu)}$ | (S12c.3) |
| $error\ in\ prefactor = prefactor * \sqrt{\left(\frac{\sigma_Y}{Y}\right)^2 + \left(\frac{\sigma_\nu}{\nu}\right)^2}$ | (S12c.4) |

The calculated values for Young's modulus and the prefactor are given in Table S12.2.

S12d. Finding Migration Molume for Use in the Elastic Strain Model:

The migration volume is defined as the change in volume of the system from the initial state to the activated state. Calculation of the volume of the fully relaxed activated state through direction optimization is not possible without some method to constrain the reaction coordinate degrees of freedom, as the system is unstable in the activated state and will relax to its initial or final state. We evaluated constrained relaxations, where only volume is allowed to relax, but felt that this approach may be inaccurate due to the many internal degrees of freedom that are constrained (this data is shown in Table S12.5). The CNEB method naturally constrains just the

reaction coordinate in the activated state but is implemented at fixed volume, and therefore does not allow relaxation of the activated state volume during the CNEB calculation. To overcome this problem, for each system and each hop, at the initial state and at the activated state, we used the bulk modulus B_0 , its derivative with respect to pressure, B_0' , the fixed volume V (common to the shared initial state and both activated states), and the pressure P at that fixed volume in the third-order Birch Murnaghan equation, Equation S12d.1, in order to calculate the expected zero-pressure volume V_0 . The Birch-Murnaghan equation is reproduced below as Equation S12d.1:

| | |
|--|----------|
| $P(V) = \frac{3B_0}{2} \left[\left(\frac{V_0}{V} \right)^{\frac{7}{3}} - \left(\frac{V_0}{V} \right)^{\frac{5}{3}} \right] \left\{ 1 + \frac{3}{4} (B_0' - 4) \left[\left(\frac{V_0}{V} \right)^{\frac{2}{3}} - 1 \right] \right\}$ | (S12d.1) |
|--|----------|

We solved for V_0 by evaluating each prospective V_0 volume in the range of 300 to 600 cubic Angstroms (for our 2x2x2 supercell size) in steps of 0.1 cubic Angstroms, paired with the known V , and took the closest match to the observed P for each case. Then we calculate the migration volume as in Equation S12d.2, with error treatment in Equation S12d.3:

| | |
|---|----------|
| $dV_{mig} = V_{0,activated} - V_{0,initial}$ | (S12d.2) |
| $\sigma_{dV_{mig}} = \sqrt{\sigma_{V_{activated}}^2 + \sigma_{V_{initial}}^2} = \sqrt{0.1^2 + 0.1^2} = 0.1\sqrt{2}$ | (S12d.3) |

Note that the values of $\sigma_{V_{activated}}$ and $\sigma_{V_{initial}}$ are taken as 0.1 \AA^3 , as this is the step size used in obtaining the values. The obtained dV_{mig} values are listed in Table S12.5.

As a different way to evaluate the elastic strain model than comparing slopes, we can supply the DFT migration barrier slopes on the left-hand side of Equation S12.4 and calculate anticipated volumes, then compare those volumes against either our Birch-Murnaghan equation

migration volumes, or our volume-only relaxation migration volumes. Figure S12.3 and Figure S12.4 show elastic-model anticipated volumes, using the Young's modulus, Poisson's ratio, and DFT-fit slopes in the elastic model Equation S12.4 in order to calculate a volume, compared to the Birch-Murnaghan calculated volumes and the volume-only relaxation calculated volumes, respectively. Figure S12.5 reproduces the elastic model analysis in the main text, but using volume-only relaxations for V_{mig} rather than Birch-Murnaghan migration volumes. Figure S12.4 and Figure S12.5 with volume-only relaxation calculations for V_{mig} are clustered somewhat closer to the guideline than the Birch-Murnaghan-calculated migration volumes, but show greater scatter in the outlier points.

Tables

Table S3.1. Supercell energy comparison for orthogonal versus non-orthogonal lattice vector c .

Table S3.1. Supercell energy comparison for orthogonal versus non-orthogonal assumption for lattice vector c .

| % strain, a and b | Fitted c fraction, greatest magnitude | Fitting equation coefficients for supercell energy (eV) | | | | Energy difference (eV), using original c fraction * sin(angle) | |
|-----------------------|---|---|--------------------------|--------------|----------|--|--------|
| | | $(c \text{ fraction})^3$ | $(c \text{ fraction})^2$ | c fraction | constant | 91.4° | 89.8° |
| -2 | 1.0268 (B=Mn) | 706.11 | -1869.1 | 1605.0 | -778.78 | 3E-05 | 1E-07 |
| 2 | 0.9838 (B=Fe) | -2231.90 | 6980.0 | -7253.2 | 2182.30 | -3E-06 | -7E-07 |

Table S5.1. U-values for GGA+U

Table S5.1. U-values for GGA versus GGA+U barriers.^{13, 39}

| B-site cation | U-J value for B-site, J=1 eV |
|---------------|------------------------------|
| Ti | 4.0 |
| V | 3.1 |
| Cr | 3.5 |
| Mn | 4.0 |
| Fe | 4.0 |
| Co | 3.3 |
| Ni | 6.4 |

Table S6.1. Magnetic moment per B-site cation from FM configuration

Table S6.1. Magnetic moment per B-site cation in LaBO₃ perovskites, when relaxed from a high-spin ferromagnetic starting configuration.^a

| B-site | Experimental (μB) | Bulk (μB) | Uncompensated | | Compensated | |
|--------|--------------------------------|------------------------|----------------------------|--------------------------------|----------------------------|--------------------------------|
| | | | Endpoint (μB) | Middle image (μB) | Endpoint (μB) | Middle image (μB) |
| Sc | 0 | 0.0 | 0.0 | 0.3 | 0.0 | 0.0 |
| Ti | 0.46 ²⁰ | 0.1 | 0.2 | 0.3 | 0.3 | 0.3 |
| V | 1.4 ⁴⁰ | 2.0 | 2.0 | 2.0 | 1.7 | 1.7 |
| Cr | 2.8 \pm 0.2 ⁴¹ | 3.0 | 3.0 | 3.3 | 3.0 | 3.0 |
| Mn | 3.9 \pm 0.2 ⁴¹ | 4.0 | 4.0 | 4.3 | 4.0 | 4.0 |
| Fe | 4.6 \pm 0.2 ⁴¹ | 3.5 | 3.3 | 3.3 | 3.5 | 3.5 |
| Co | 2 ^{b42} | 1.6 | 1.4 | 1.3 | 1.7 | 1.8 |
| Ni | 1 ^{c43} | 0.3 | 0.1 | 0.3 | 0.4 | 0.2 |
| Ga | 0 | 0.0 | 0.0 | 0.0 | 0.0 | 0.0 |

^a The full relaxation was followed by a static calculation. The calculated magnetic moment for the B-site cation in the bulk or endpoint is taken by dividing the total supercell magnetic moment by 8. This procedure re-attributes to the B-site cations the small moments which the VASP calculations sometimes put onto the La³⁺ and O²⁻ ions. The magnetic moment for the first endpoint was in all cases the same as the magnetic moment for the second endpoint, to the accuracy displayed here.

^b According to Saitoh et al., LaCoO₃ is nonmagnetic at 0K to paramagnetic at 90K, with a purported transition from t_{2g}^6 to $t_{2g}^5 e_g^1$, which would give a moment of 2 μB per Co ion.

^c According to Sreedhar et al., the configuration is $t_{2g}^6 e_g^1$.

Table S6.2. Effect of AFM structure on LaXO3 calculations

Table S6.2. Effect of antiferromagnetic structure on LaXO3 calculations, using a 4x4x4M kpoint mesh.

| B-site | Exper. AFM | $E_{\text{bulk, AFM}} < E_{\text{bulk, FM}}^b$ | $E_{\text{mig, AFM}} - E_{\text{mig, FM}}^a$ (compensated) | $E_{\text{mig, AFM}} - E_{\text{mig, FM}}$ (uncompensated) | Néel Temp. (K) ⁴⁴ |
|--------|--|--|---|---|------------------------------|
| Sc | not magnetic ¹⁸ | N/A | N/A | N/A | (not listed) |
| Ti | G-type ⁴⁵ | No | N/A | N/A | paramagnetic |
| V | C-type, cited ¹⁸ | - 0.22 | -0.03 | 0.04 | 137 |
| V | G-type ⁴⁶ | No | N/A | -0.11 | 137 |
| Cr | G-type ⁴¹ | - 0.72 | -0.15 | 0.36 | 320 |
| Mn | A-type ⁴¹ | No | N/A | N/A | 100 |
| Mn | G-type (for consistency) | No | N/A | N/A | 100 |
| Fe | G-type ⁴¹ | - 0.30 | -0.11 | -0.39 | 750 |
| Co | None (<90 K) to paramagnetic ⁴² | N/A | N/A | N/A | (not listed) |
| Ni | None (<15K) to paramagnetic ⁴³ | N/A | N/A | N/A | paramagnetic |
| Ga | not magnetic ⁴⁷ | N/A | N/A | N/A | (not listed) |

^a Migration barriers were taken from 3-image CNEB calculations

^b If the relaxed bulk energy calculated in VASP with an antiferromagnetic high-spin starting configuration was lower than the relaxed bulk energy calculated with a ferromagnetic starting configuration, then more AFM calculations were pursued.

Table S6.3. Literature values for comparison with LaXO3 barriers.

Table S6.3. Literature values for Figure S6.1.

| Actual material | Approx. material | Temp. (°C) | Emig (eV) | Source |
|------------------------|------------------|------------|-----------|--------|
| La0.9Sr0.1Sc0.9Mg0.1O3 | LaScO3 | 1000 | 0.50 | 22 |
| La0.7Ca0.3CrO3 | LaCrO3 | 900-1000 | 0.81 | 48 |
| La0.79Sr0.20MnO3 | LaMnO3 | 700-860 | 0.73 | 49 |
| La0.8Sr0.2MnO3 | LaMnO3 | 850-1000 | 1.47 | 24 |
| LaFeO3 | LaFeO3 | 900-1100 | 0.77 | 28 |
| La0.9Sr0.1FeO3 | LaFeO3 | 900-1100 | 0.82 | 28 |
| La0.75Sr0.25FeO3 | LaFeO3 | 900-1050 | 1.18 | 28 |
| LaCoO3 | LaCoO3 | 850-1000 | 0.78 | 50 |
| LaCoO3 | LaCoO3 | 850-1000 | 0.80 | 28 |
| La0.9Sr0.1CoO3 | LaCoO3 | 800-1000 | 0.82 | 28 |
| La0.9Sr0.1Ga0.9Mg0.1O3 | LaGaO3 | 1000 | 0.60 | 22 |

Table S7.1. Difference between electron-removal compensated migration barriers and doped migration barriers.

Table S7.1. Difference between electron-removal compensated migration barriers and doped migration barriers. This hop is from O29 to O30 (unstrained).

| B-site | Barrier for LaBO ₃ compensated - barrier for LaBO ₃ doped (eV) | With shift from mean of compensated minus doped barrier (eV) |
|----------------------|--|--|
| Sc | -0.07 | 0.07 |
| Ti | -0.12 | 0.02 |
| V | -0.11 | 0.03 |
| Cr | -0.21 | -0.07 |
| Mn | -0.25 | -0.11 |
| Fe | -0.24 | -0.10 |
| Co | -0.10 | 0.04 |
| Ni | -0.07 | 0.07 |
| Ga | -0.08 | 0.06 |
| <i>Largest value</i> | <i>-0.25</i> | <i>-0.11</i> |
| <i>Mean value</i> | <i>-0.14</i> | <i>0.00</i> |
| <i>RMS value</i> | <i>0.16</i> | <i>0.07</i> |

Table S7.2 In-plane and out-of-plane slopes for $\text{La}_{0.75}\text{Sr}_{0.25}\text{BO}_3$ supercells, compared with undoped slopes.

Table S7.2 In-plane and out-of-plane slopes for $\text{La}_{0.75}\text{Sr}_{0.25}\text{BO}_3$ supercells, compared with undoped slopes. In-plane hop is from oxygen position o31 to o30 (see Figure S2.1). Out-of-plane hop is from oxygen position o29 to o30. Cross-body diagonal dopant positions are a1 and a8. Cross-face diagonal dopant positions are a2 and a8. In-line dopant positions are a4 and a8.

| | B-site cation | Dopant position: | Slope of migration barrier versus strain (meV/% strain) +/- fitting error | | | |
|------------------|---------------|------------------|---|------------|-------------|---|
| | | | Cross-body | Cross-face | In-line | No dopants (electron-removal compensated) |
| In-plane hop | Sc | | -24 +/- 1 | -26 +/- 1 | -31 +/- 1 | -36 +/- 3 |
| | Cr | | -91 +/- 1 | -90 +/- 1 | -92 +/- 1 | -85 +/- 0 |
| | Mn | | -106 +/- 9 | -94 +/- 9 | -111 +/- 16 | -64 +/- 4 |
| Out-of-plane hop | Sc | | -34 +/- 3 | -31 +/- 1 | -47 +/- 2 | -52 +/- 2 |
| | Cr | | -111 +/- 2 | -98 +/- 1 | -110 +/- 1 | -122 +/- 1 |
| | Mn | | -68 +/- 12 | -73 +/- 4 | -91 +/- 6 | -77 +/- 3 |

Table S8.1. Out-of-plane slopes and slope error

Table S8.1. Out-of-plane slopes and slope error for Figure S8.1.

| B-site cation | Out-of-plane slope fit to DFT (meV/% strain) | Out-of-plane slope error (meV/% strain) |
|---------------|--|---|
| Sc | -52 | 2 |
| Ti | -73 | 3 |
| V | -115 | 25 |
| Cr | -122 | 1 |
| Mn | -77 | 3 |
| Fe | -79 | 9 |
| Co | -80 | 7 |
| Ni | -21 | 10 |
| Ga | -64 | 0.4 |

Table S8.2. Eight migration barriers in LaXO_3 for several B-site cations.

Table S8.2. Eight migration barriers in LaXO_3 (compensation state indicated), moving the vacancy from atomic position 30 (an arbitrary choice for convenience) to the position indicated, and using a single image except where noted and a 4x4x4M kmesh. Barriers and range are

measured in eV. The in-plane hop discussed in the main text and the out-of-plane hop discussed in the Supporting Information are marked in bold.

| Oxygen position | Sc uncompe nsated | Sc compensated | Ti uncomp. | V (3 images) uncomp. | Cr uncomp. | Mn (3 images) uncomp. | Fe uncomp. |
|-------------------|-------------------|----------------|-------------|----------------------|-------------|-----------------------|-------------|
| In-plane hops | | | | | | | |
| 30 to 19 | 2.33 | 0.85 | 1.76 | 1.80 | 1.89 | 1.20 | 0.95 |
| 30 to 25 | 1.80 | 0.53 | 1.67 | 1.66 | 1.85 | 1.19 | 0.92 |
| 30 to 31 | 1.73 | 0.49 | 1.56 | 1.62 | 1.72 | 0.92 | 0.83 |
| 30 to 37 | 2.03 | 0.75 | 1.66 | 1.72 | 1.79 | 1.16 | 0.95 |
| Out-of-plane hops | | | | | | | |
| 30 to 17 | 1.97 | 0.53 | 1.61 | 1.60 | 1.86 | 1.19 | 0.86 |
| 30 to 20 | 1.96 | 0.46 | 1.61 | 1.64 | 1.79 | 0.98 | 0.83 |
| 30 to 29 | 1.96 | 0.46 | 1.61 | 1.64 | 1.72 | 0.98 | 0.81 |
| 30 to 32 | 1.97 | 0.53 | 1.61 | 1.60 | 1.84 | 1.09 | 0.86 |
| <i>Range (eV)</i> | <i>0.60</i> | <i>0.39</i> | <i>0.20</i> | <i>0.20</i> | <i>0.17</i> | <i>0.28</i> | <i>0.14</i> |

Table S12.1. Comparing PV_{mig} for constant pressure and E_{mig} for constant volume

Table S12.1. Comparing PV_{mig} for constant pressure and E_{mig} for constant volume, from LaCrO_3 , in-plane hop. The pressure given is that of the perfect strained cell. The migration volume was calculated using the Birch-Murnaghan equation procedure in Section S12d. The ‘‘Schichtel expected’’ pressure value is calculated from Equation S12.1, given the LaCrO_3 prefactor from Table S12.2. The ΔE_{mig} value is taken as the difference between the strained E_{mig} and the zero-strain E_{mig} (0.90 eV). The Schichtel expected ΔG_{mig} is calculated from Equation S12.2, given both the LaCrO_3 prefactor from Table S12.2 and the migration volume in this table.

| Epitaxial strain | P (kbar) | V_{mig} (\AA^3) | PV_{mig} (eV) | Schichtel expected P (kbar) | E_{mig} , (eV) | ΔE_{mig} (eV) | Schichtel expected ΔG_{mig} (eV) |
|------------------|------------|------------------------------|-----------------|-------------------------------|------------------|-----------------------|--|
| -0.02 | 43.89 | 4.5 | 0.12 | 46.12 | 1.06 | 0.161 | 0.13 |
| 0.02 | -45.08 | 4.2 | -0.12 | -46.12 | 0.73 | -0.178 | -0.12 |

Table S12.2. Strained-bulk calculated Poisson's ratio, Young's modulus, and prefactor, with errors.

Table S12.2. Strained-bulk calculated Poisson's ratio, Young's modulus, and prefactor, with errors.

| B-site cation | Poisson's ratio | Error in ν | Y (eV/Å ³) | Error in Y (eV/Å ³) | Prefactor (eV/Å ³) | Error in prefactor (eV/Å ³) |
|---------------|-----------------|----------------|--------------------------|-----------------------------------|--------------------------------|---|
| Sc | 0.290 | 0.001 | 1.23 | 0.02 | 1.16 | 0.02 |
| Ti | 0.292 | 0.003 | 1.37 | 0.03 | 1.29 | 0.03 |
| V | 0.311 | 0.087 | 1.29 | 0.59 | 1.25 | 0.67 |
| Cr | 0.266 | 0.001 | 1.59 | 0.02 | 1.44 | 0.02 |
| Mn | 0.350 | 0.003 | 0.95 | 0.04 | 0.97 | 0.04 |
| Fe | 0.321 | 0.008 | 1.03 | 0.06 | 1.02 | 0.07 |
| Co | 0.311 | 0.022 | 1.17 | 0.15 | 1.13 | 0.17 |
| Ni | 0.386 | 0.015 | 0.76 | 0.20 | 0.82 | 0.21 |
| Ga | 0.321 | 0.000 | 1.14 | 0.02 | 1.12 | 0.02 |

Table S12.3. Bulk modulus values and errors

Table S12.3. Bulk modulus values and errors

| B-site cation | B_0 (kbar) | error in B_0 (kbar) | B_0' | B_0 (GPa) | B_0 (eV/Å ³) | error in B_0 (eV/Å ³) |
|---------------|--------------|-----------------------|--------|-------------|----------------------------|-------------------------------------|
| Sc | 1572 | 8 | 4.12 | 157.2 | 0.981 | 0.005 |
| Ti | 1761 | 10 | 4.25 | 176.1 | 1.099 | 0.006 |
| V | 1820 | 6 | 4.52 | 182.0 | 1.136 | 0.004 |
| Cr | 1805 | 9 | 4.09 | 180.5 | 1.127 | 0.006 |
| Mn | 1689 | 16 | 3.93 | 168.9 | 1.054 | 0.010 |
| Fe | 1539 | 17 | 3.37 | 153.9 | 0.961 | 0.010 |
| Co | 1652 | 31 | 2.46 | 165.2 | 1.031 | 0.020 |
| Ni | 1766 | 72 | 3.99 | 176.6 | 1.102 | 0.045 |
| Ga | 1692 | 10 | 4.28 | 169.2 | 1.056 | 0.006 |

Table S12.4. Vacancy effects on bulk modulus and elastic model

Table S12.4. Vacancy effects on bulk modulus and elastic model. The bulk modulus was calculated using a series of static calculations at different volumes under the specified conditions.

| Condition | B=Mn | | | B=Cr | | |
|--------------------------------------|-------------------------------|-----------------------------|----------------------------------|-------------------------------|-----------------------------|----------------------------------|
| | B_0 (eV/Å ³) | E (eV/Å ³) | prefactor (2/3)*E/(1- ν) | B_0 (eV/Å ³) | E (eV/Å ³) | prefactor (2/3)*E/(1- ν) |
| Undefected bulk | 1.05 | 0.95 | 0.97 | 1.13 | 1.58 | 1.44 |
| Initial state, compensated vacancy | 1.22 | 1.10 | 1.13 | 1.31 | 1.83 | 1.67 |
| Transition state, compensated | 1.14 | 1.03 | 1.05 | 1.21 | 1.70 | 1.55 |
| Initial state, uncompensated vacancy | 1.08 | 0.97 | 1.00 | 1.10 | 1.55 | 1.41 |
| Transition state, uncompensated | 1.02 | 0.92 | 0.95 | 1.07 | 1.50 | 1.36 |

Table S12.5. Migration volumes, calculated with BM equation or allowing volume-only relaxation

Table S12.5. Migration volumes, calculated with the Birch-Murnaghan equation (first two numeric columns) and calculated by allowing a volume-only relaxation (last two columns)

| B-site cation | dVmig IP, Birch-Murn. | dVmig OOP, Birch-Murn. | dVmig IP, volume relaxation (not used) | dVmig OOP, volume relaxation (not used) |
|---------------|-----------------------|------------------------|--|---|
| Sc | 2.2 | 2.8 | 3.0 | 3.9 |
| Ti | 3.1 | 3.7 | 3.9 | 4.7 |
| V | 6.1 | 9.5 | 11.4 | 5.4 |
| Cr | 4.3 | 4.6 | 5.8 | 6.3 |
| Mn | 3.4 | 3.8 | 4.7 | 5.3 |
| Fe | 7.1 | 7.3 | 8.3 | 8.2 |
| Co | 3.8 | 4.1 | 5.2 | 6.0 |
| Ni | 2.9 | 2.7 | 5.4 | 5.5 |
| Ga | 2.5 | 3.4 | 3.9 | 5.2 |

Figures

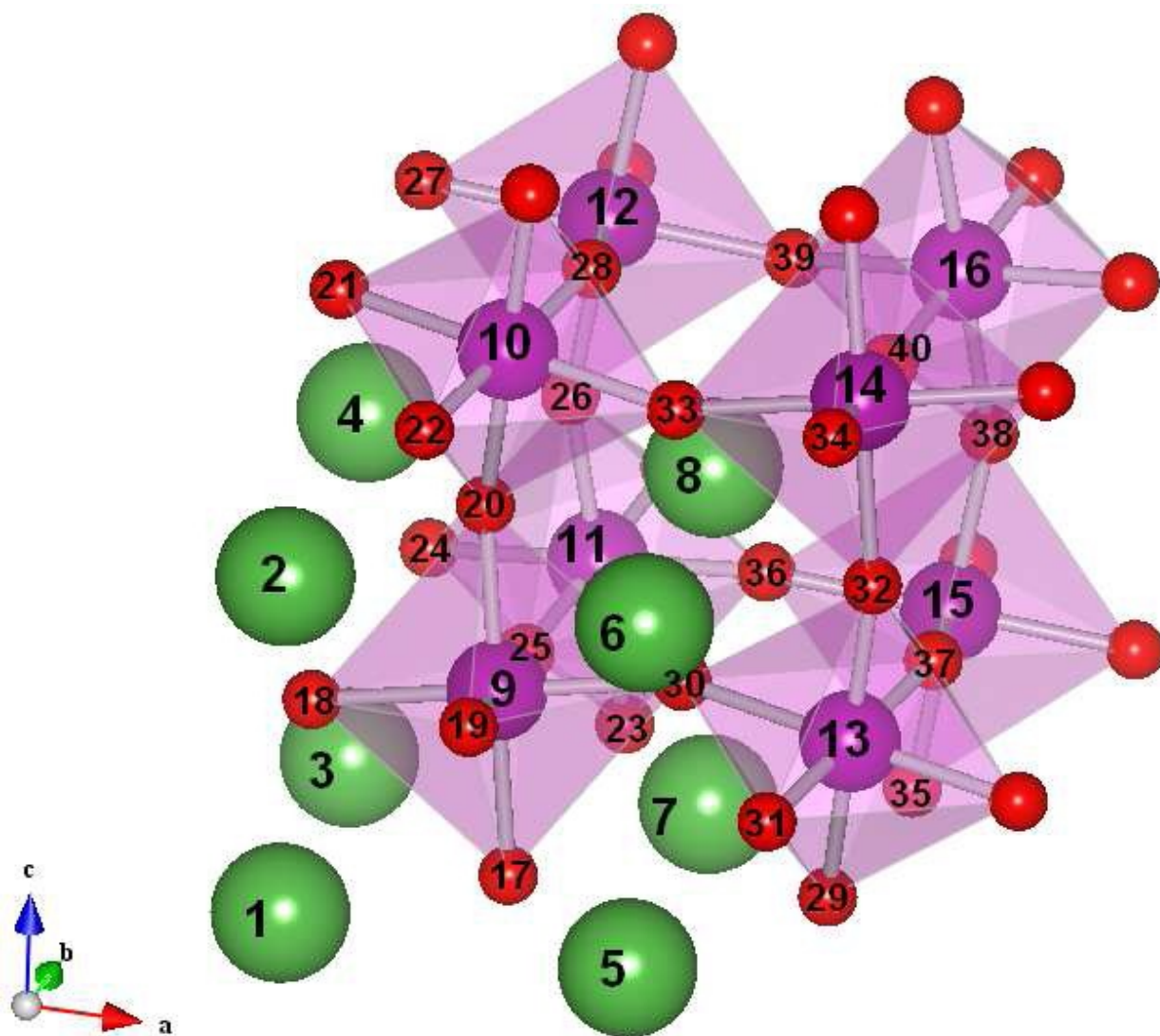


Figure S2.1. Numbered atomic positions.

Figure S2.1. Numbered atomic positions, taken from the relaxed LaMnO₃ bulk, pictured with atomic radii for clarity.

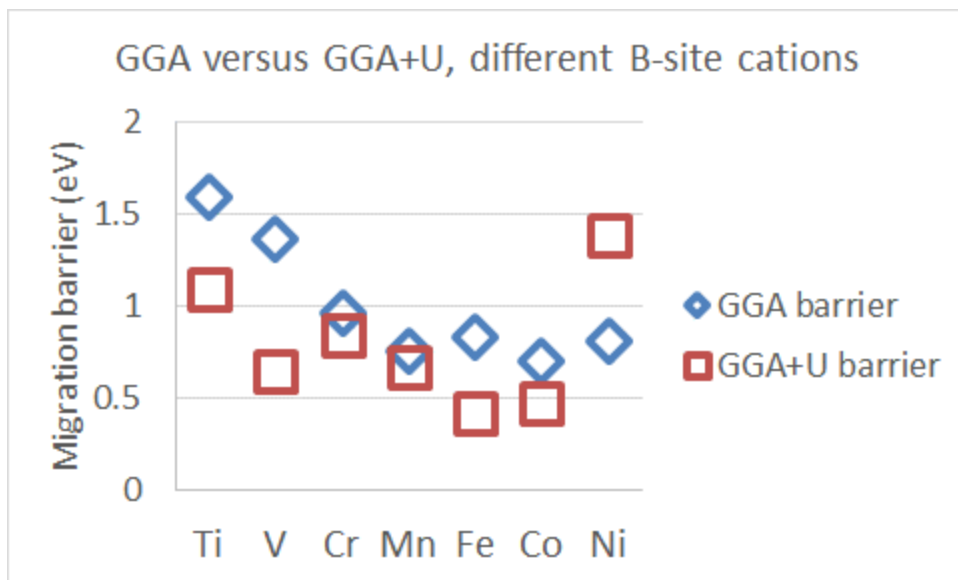


Figure S5.1. GGA versus GGA+U no-strain migration barriers.

Figure S5.1. GGA versus GGA+U no-strain migration barriers.

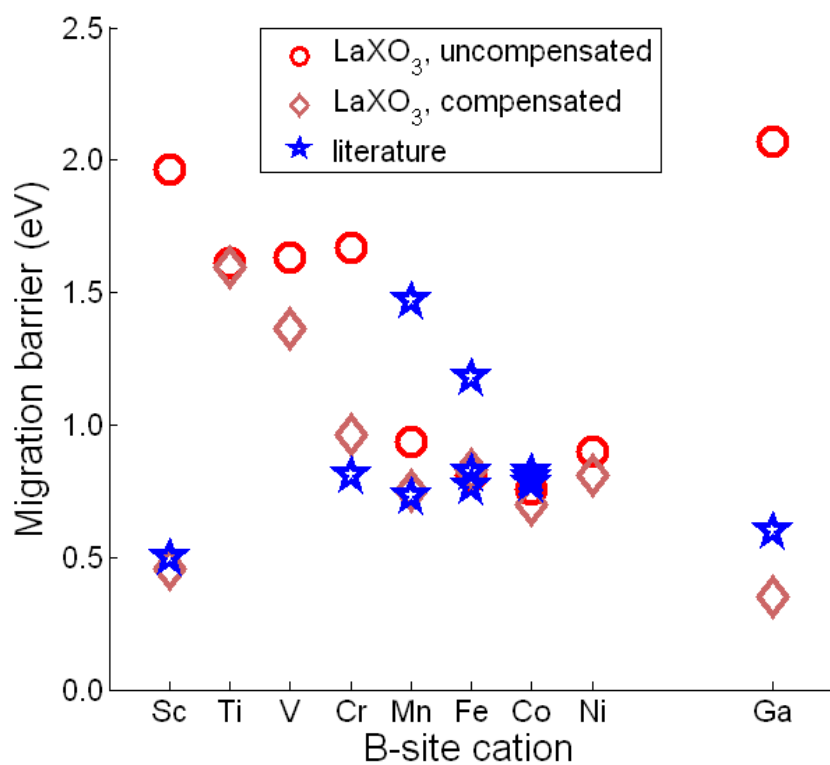


Figure S6.1. Literature compared with LaXO₃ barriers.

Figure S6.1. Literature compared with LaXO₃ uncompensated (reduced B-site cations) and compensated (all B-site cations nominally 3+ due to removal of extra electrons along with oxygen atoms) systems. Literature values are given in Table S6.3.

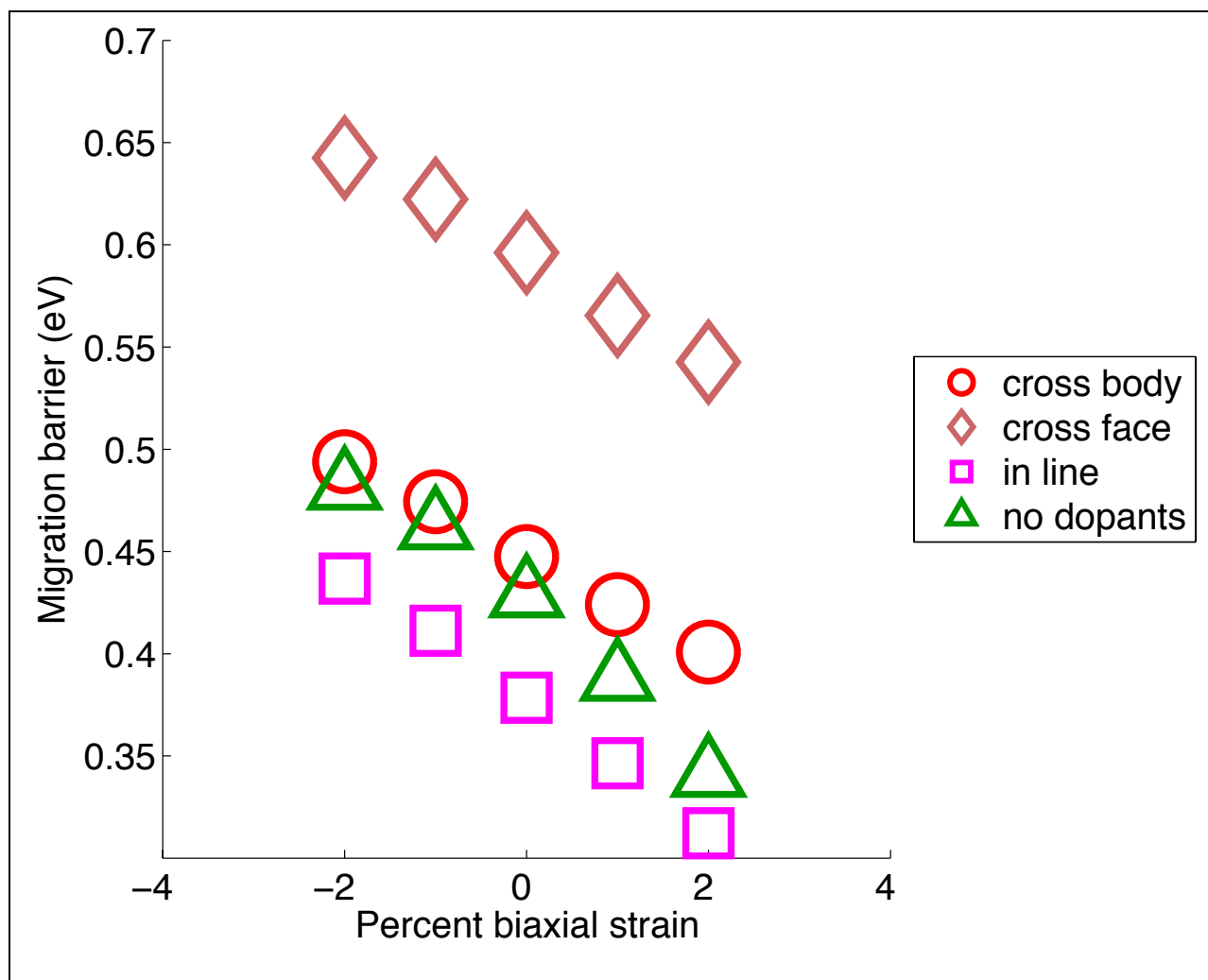


Figure S7.1 LaScO_3 and $\text{La}_{0.75}\text{Sr}_{0.25}\text{ScO}_3$ migration barrier versus strain, in-plane hop

Figure S7.1 LaScO_3 and $\text{La}_{0.75}\text{Sr}_{0.25}\text{ScO}_3$ migration barrier versus strain, in-plane hop from oxygen position o31 to o30 (see Figure S2.1). Cross-body diagonal dopant positions are a1 and a8. Cross-face diagonal dopant positions are a2 and a8. In-line dopant positions are a4 and a8.

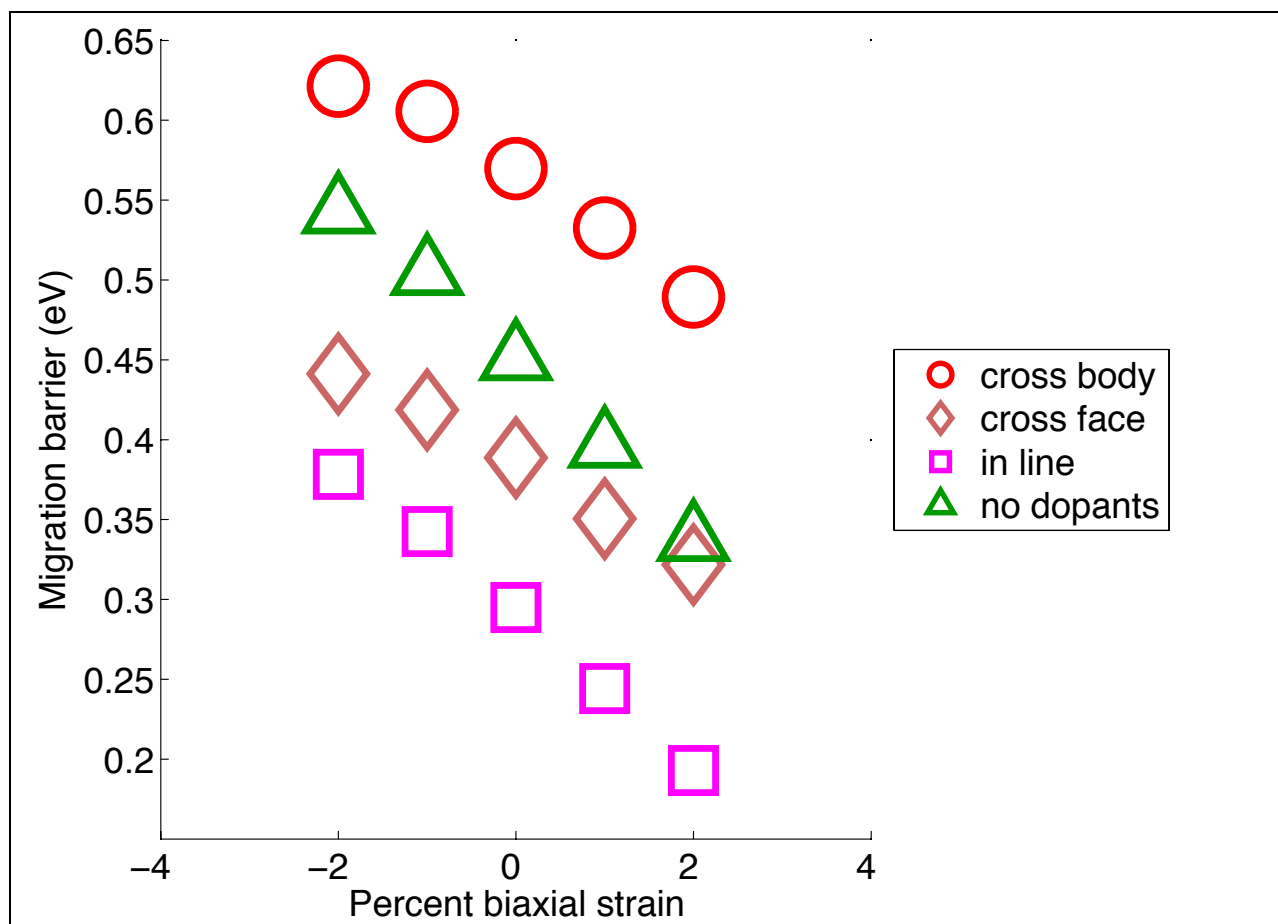


Figure S7.2 LaScO₃ and La_{0.75}Sr_{0.25}ScO₃ migration barrier versus strain, out-of-plane hop

Figure S7.2 LaScO₃ and La_{0.75}Sr_{0.25}ScO₃ migration barrier versus strain, out-of-plane hop from oxygen position o29 to o30 (see Figure S2.1). Cross-body diagonal dopant positions are a1 and a8. Cross-face diagonal dopant positions are a2 and a8. In-line dopant positions are a4 and a8.

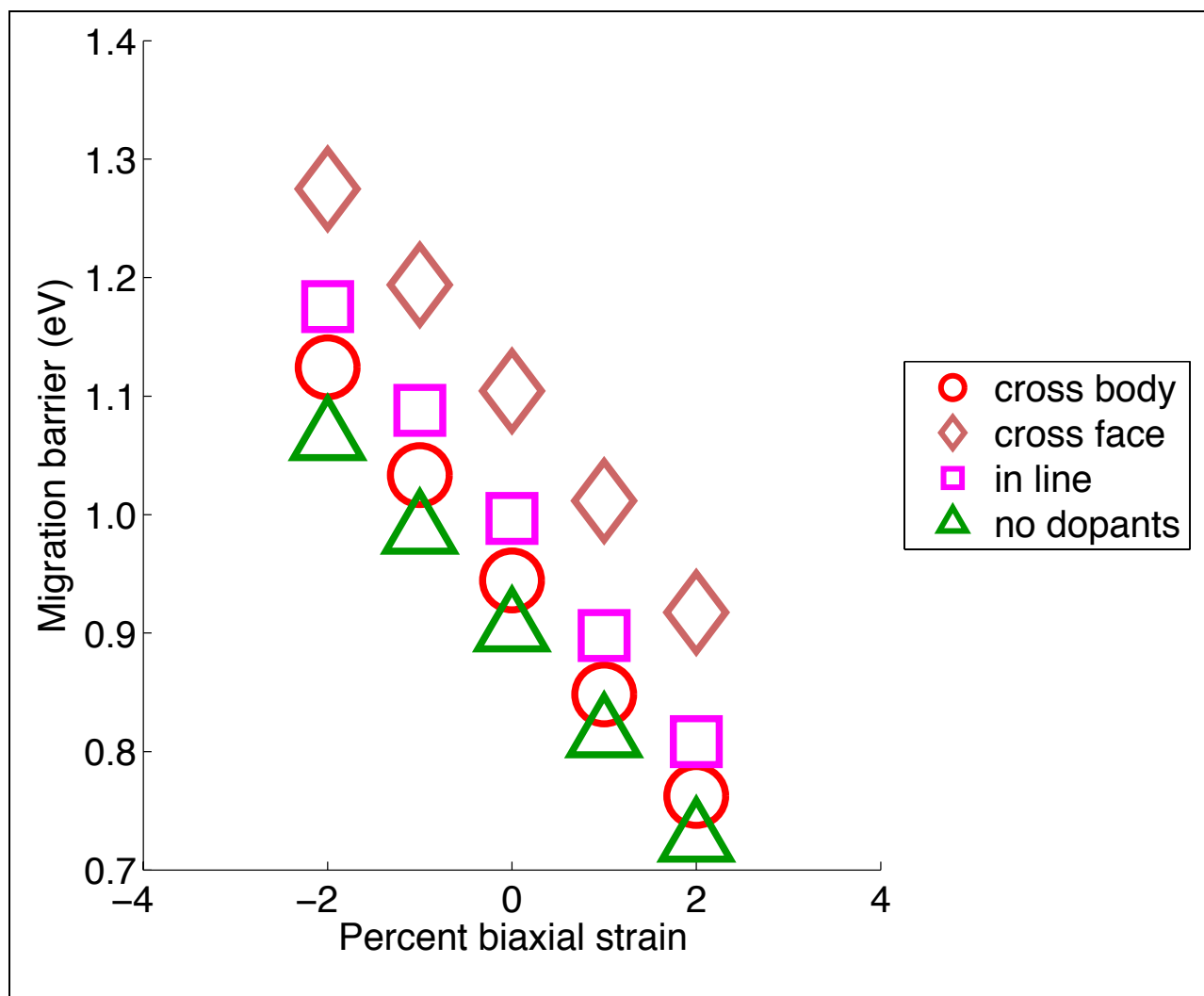


Figure S7.3 LaCrO_3 and $\text{La}_{0.75}\text{Sr}_{0.25}\text{CrO}_3$ migration barrier versus strain, in-plane hop

Figure S7.3 LaCrO_3 and $\text{La}_{0.75}\text{Sr}_{0.25}\text{CrO}_3$ migration barrier versus strain, in-plane hop from oxygen position o31 to o30 (see Figure S2.1). Cross-body diagonal dopant positions are a1 and a8. Cross-face diagonal dopant positions are a2 and a8. In-line dopant positions are a4 and a8.

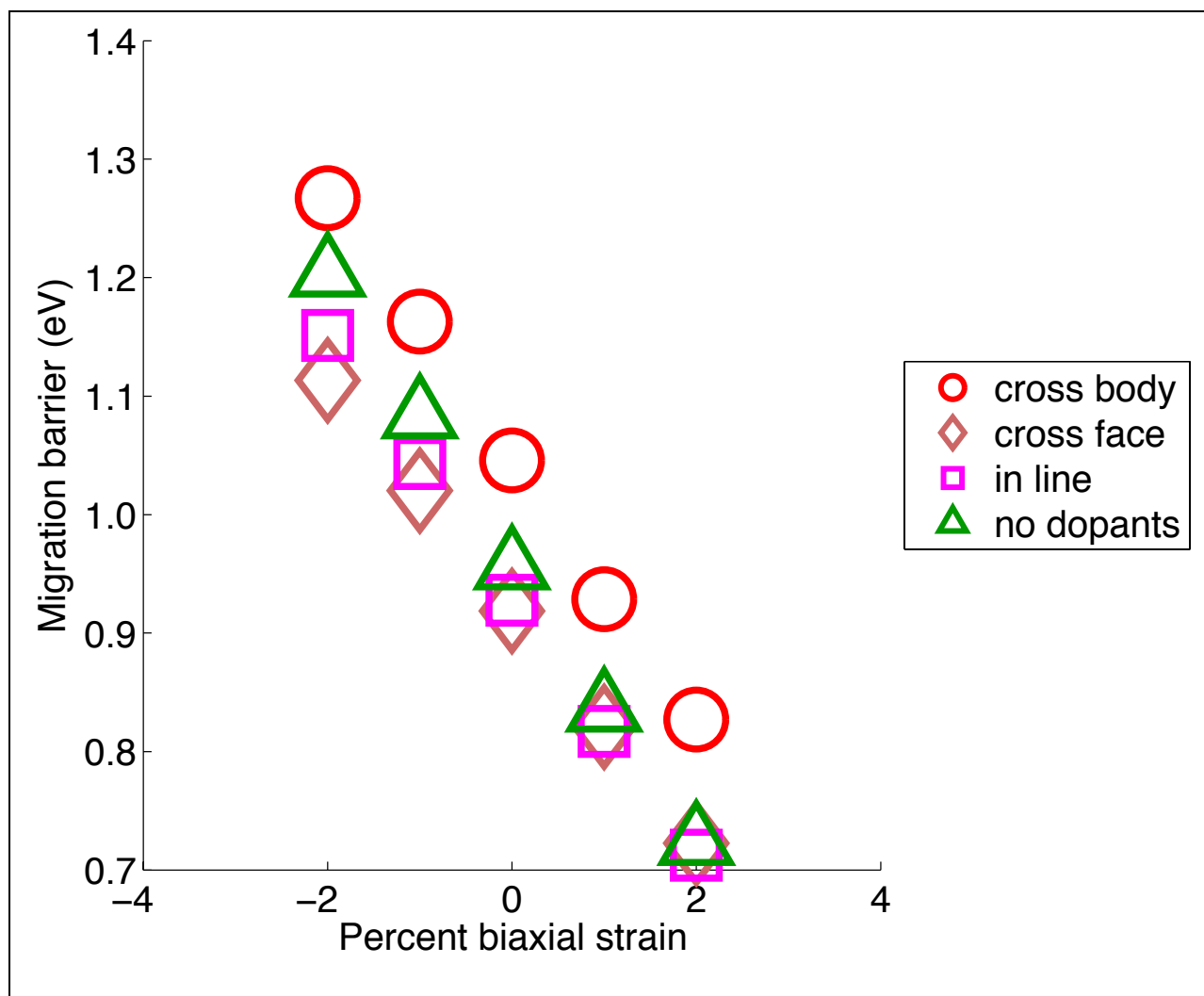


Figure S7.4 LaCrO_3 and $\text{La}_{0.75}\text{Sr}_{0.25}\text{CrO}_3$ migration barrier versus strain, out-of-plane hop

Figure S7.4 LaCrO_3 and $\text{La}_{0.75}\text{Sr}_{0.25}\text{CrO}_3$ migration barrier versus strain, out-of-plane hop from oxygen position o29 to o30 (see Figure S2.1). Cross-body diagonal dopant positions are a1 and a8. Cross-face diagonal dopant positions are a2 and a8. In-line dopant positions are a4 and a8.

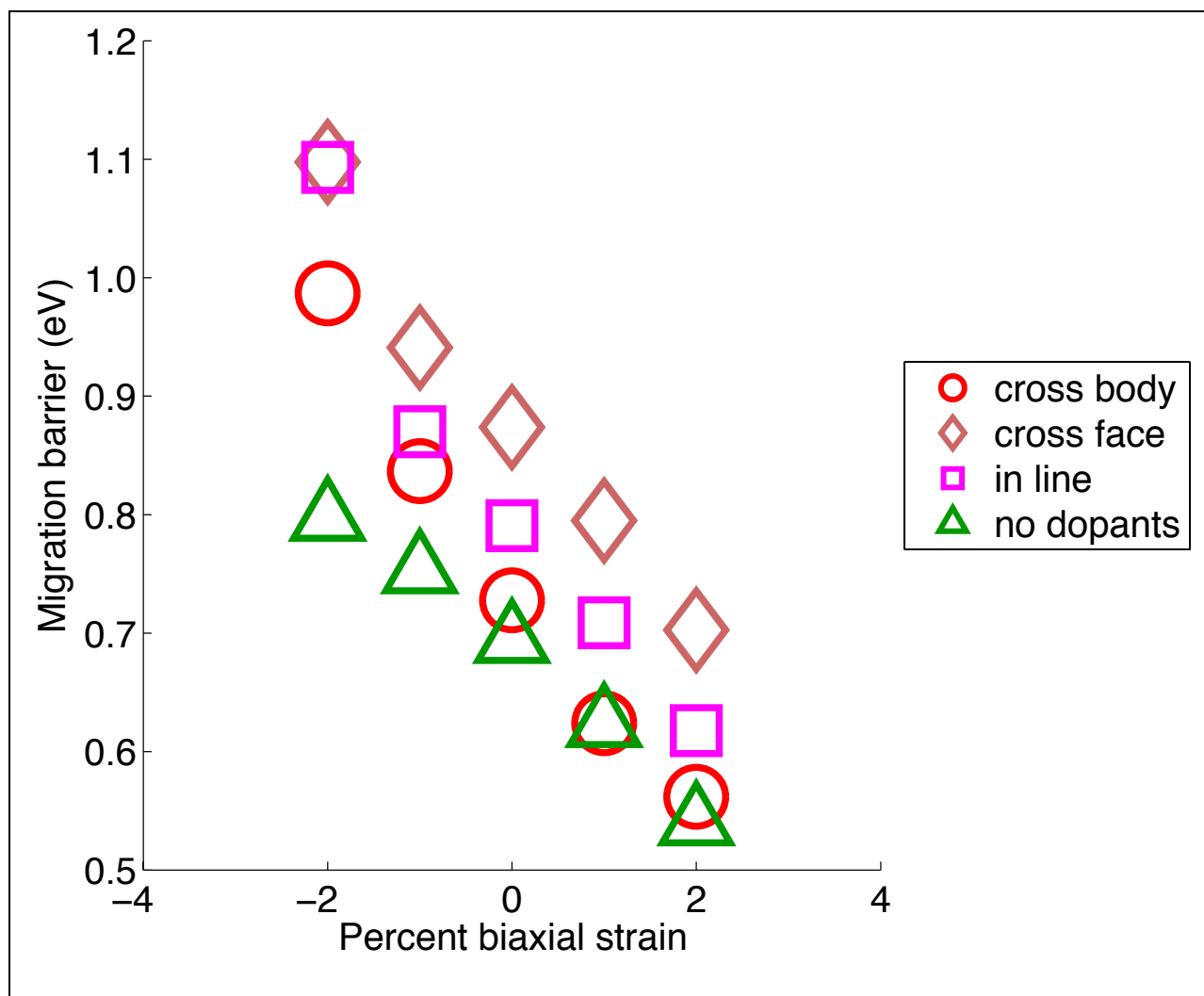


Figure S7.5 LaMnO_3 and $\text{La}_{0.75}\text{Sr}_{0.25}\text{MnO}_3$ migration barrier versus strain, in-plane hop

Figure S7.5 LaMnO_3 and $\text{La}_{0.75}\text{Sr}_{0.25}\text{MnO}_3$ migration barrier versus strain, in-plane hop from oxygen position o31 to o30 (see Figure S2.1). Cross-body diagonal dopant positions are a1 and a8. Cross-face diagonal dopant positions are a2 and a8. In-line dopant positions are a4 and a8.

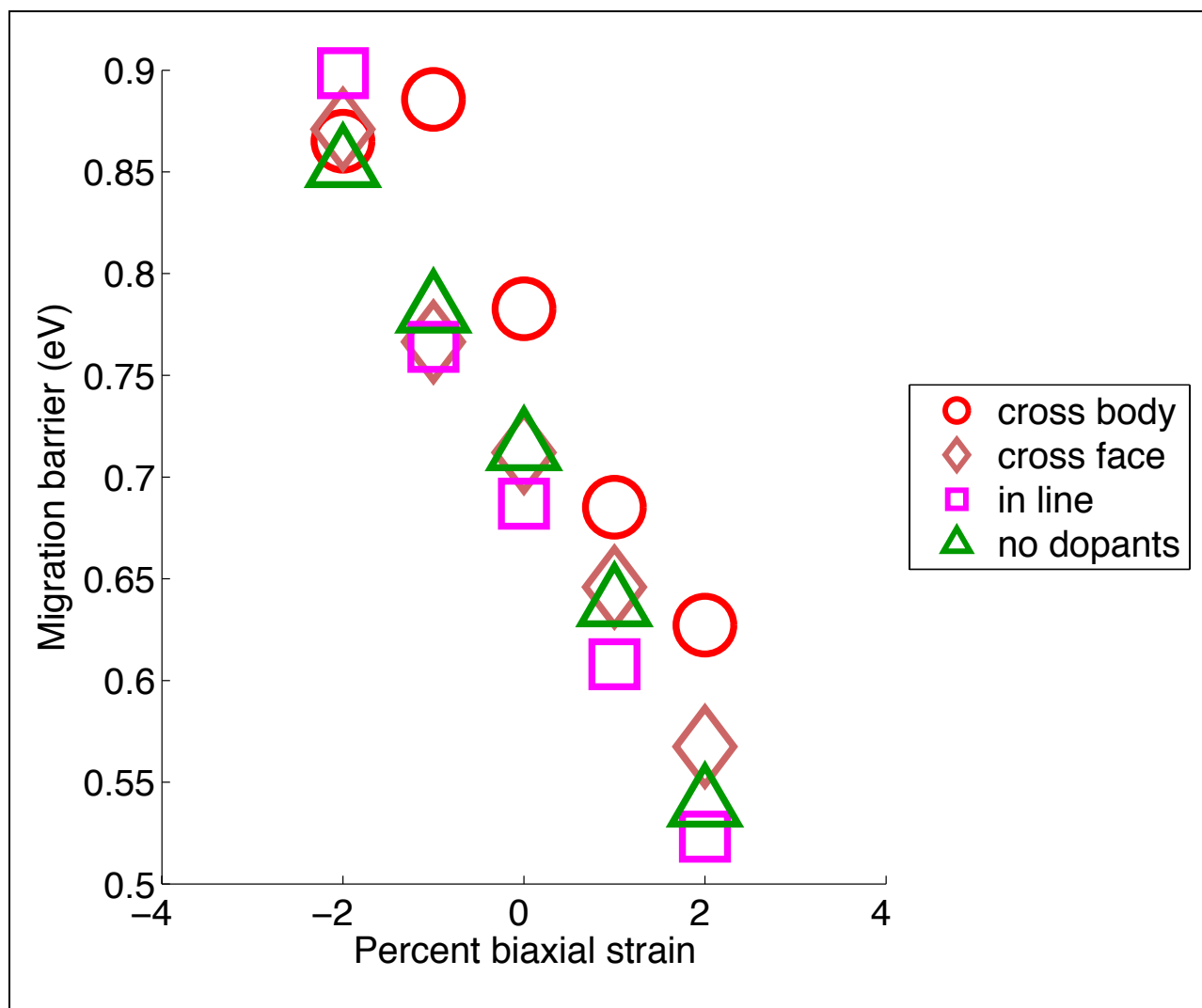


Figure S7.6 LaMnO_3 and $\text{La}_{0.75}\text{Sr}_{0.25}\text{MnO}_3$ migration barrier versus strain, out-of-plane hop

Figure S7.6 LaMnO_3 and $\text{La}_{0.75}\text{Sr}_{0.25}\text{MnO}_3$ migration barrier versus strain, out-of-plane hop from oxygen position o29 to o30 (see Figure S2.1). Cross-body diagonal dopant positions are a1 and a8. Cross-face diagonal dopant positions are a2 and a8. In-line dopant positions are a4 and a8.

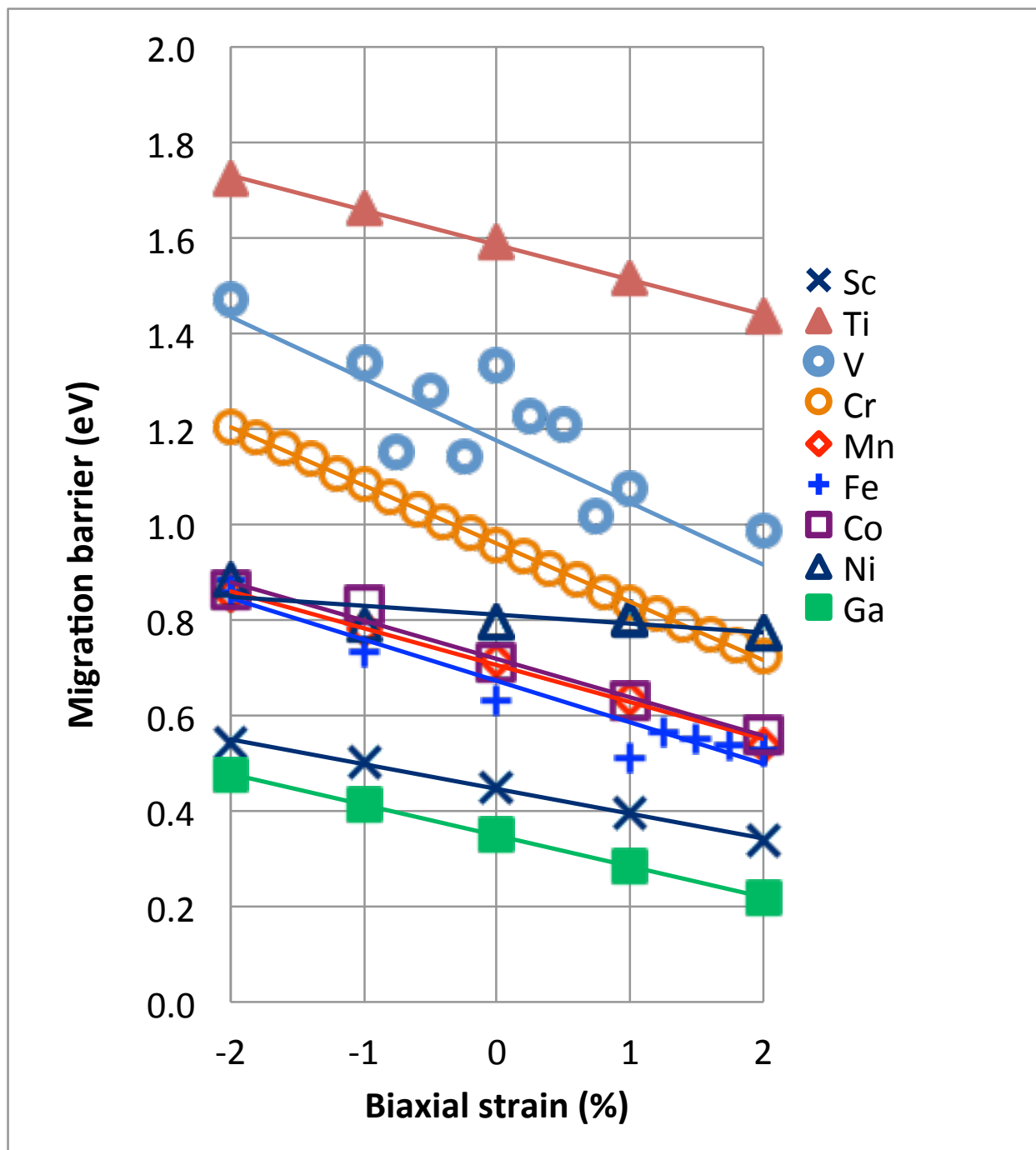


Figure S8.1. Migration barrier versus strain, out-of-plane hop

Figure S8.1. Change in migration barrier versus biaxial strain for a selected out-of-plane hop for all systems (o29 to o30).

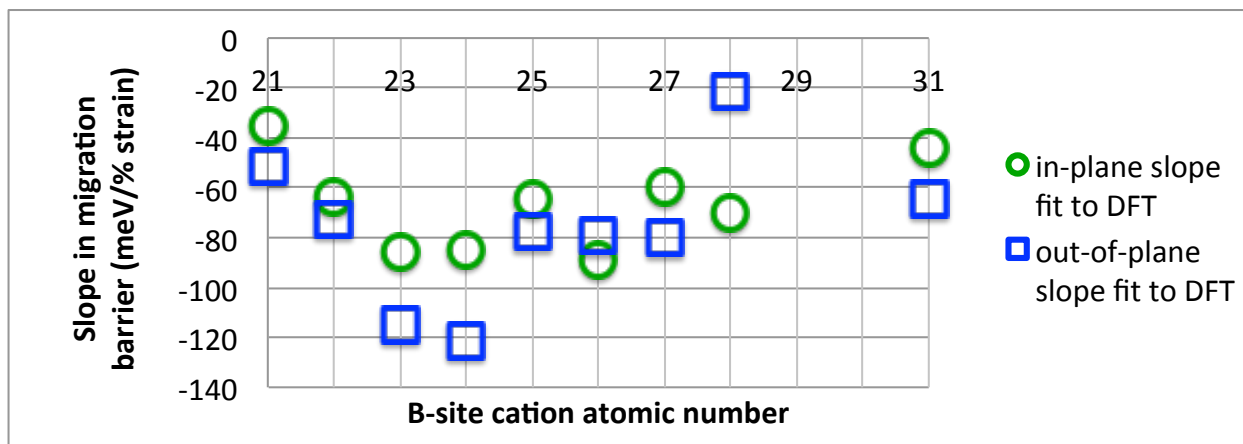


Figure S8.2. Migration barrier versus strain slopes for in-plane and out-of-plane hops.

Figure S8.2. Slopes in migration barrier for in-plane and out-of-plane hops across all systems, plotted by B-site cation atomic number. These slope values correspond to Table 1 in the main text and Table S8.1. No clear trend with B-site atomic number is evident.

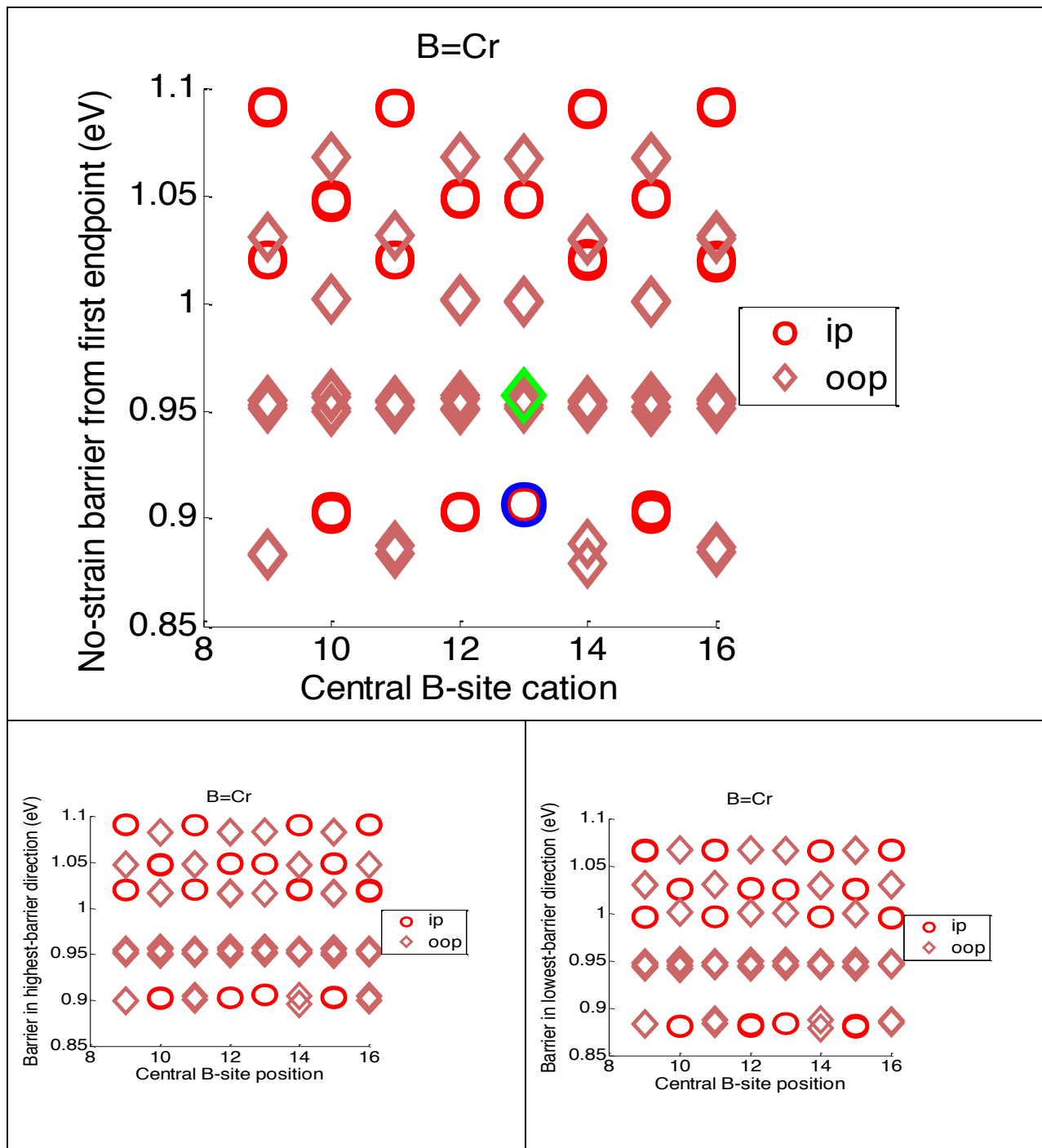


Figure S8.3. $LaCrO_3$ barriers, all hops.

Figure S8.3. LaCrO_3 calculated barriers, all oxygen hops, all octahedra, with a total of 96 barriers (12 symmetry distinct) for each strain case. The no-strain case is shown here. Several barriers overlap, reducing the apparent number of points. The top plot shows the hop energy from the initial to the final endpoint, where the out-of-plane and in-plane hops calculated consistently for all systems are highlighted in green and blue, respectively. The smaller plots show the energies for hops in the maximum hop energy (bottom left plot) and minimum hop energy (bottom right plot) directions. The change in energy associated with hopping in the opposite direction is never more than 30 meV

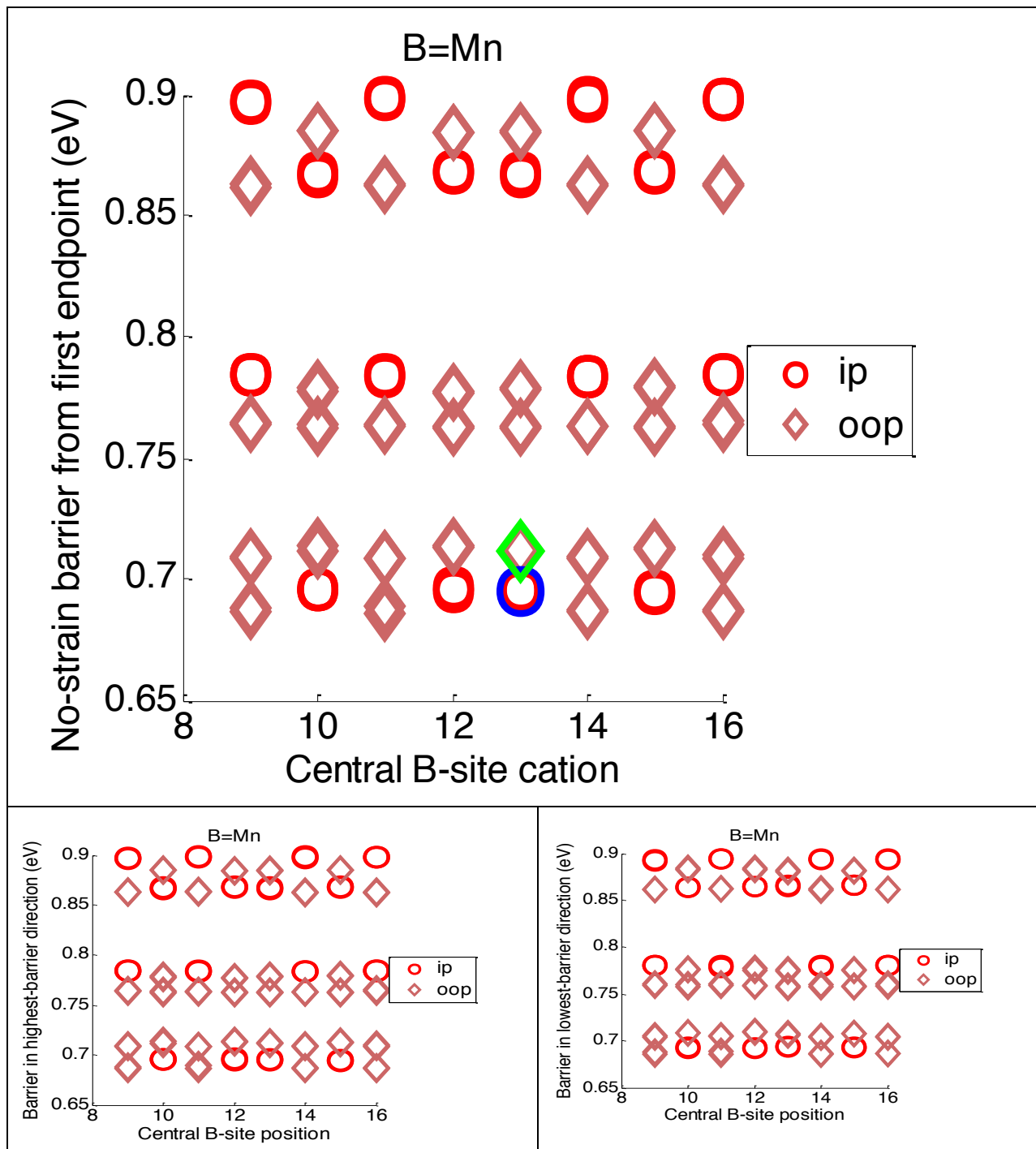


Figure S8.4. LaMnO3 barriers, all hops.

Figure S8.4. LaMnO_3 calculated barriers, all oxygen hops, all octahedra, with a total of 96 barriers (12 symmetry distinct) for each strain case. The no-strain case is shown here. Several barriers overlap, reducing the apparent number of points. The top plot shows the hop energy from the initial to the final endpoint, where the out-of-plane and in-plane hops calculated consistently for all systems are highlighted in green and blue, respectively. The smaller plots show the energies for hops in the maximum hop energy (bottom left plot) and minimum hop energy (bottom right plot) directions. The change in energy associated with hopping in the opposite direction is never more than 30 meV.

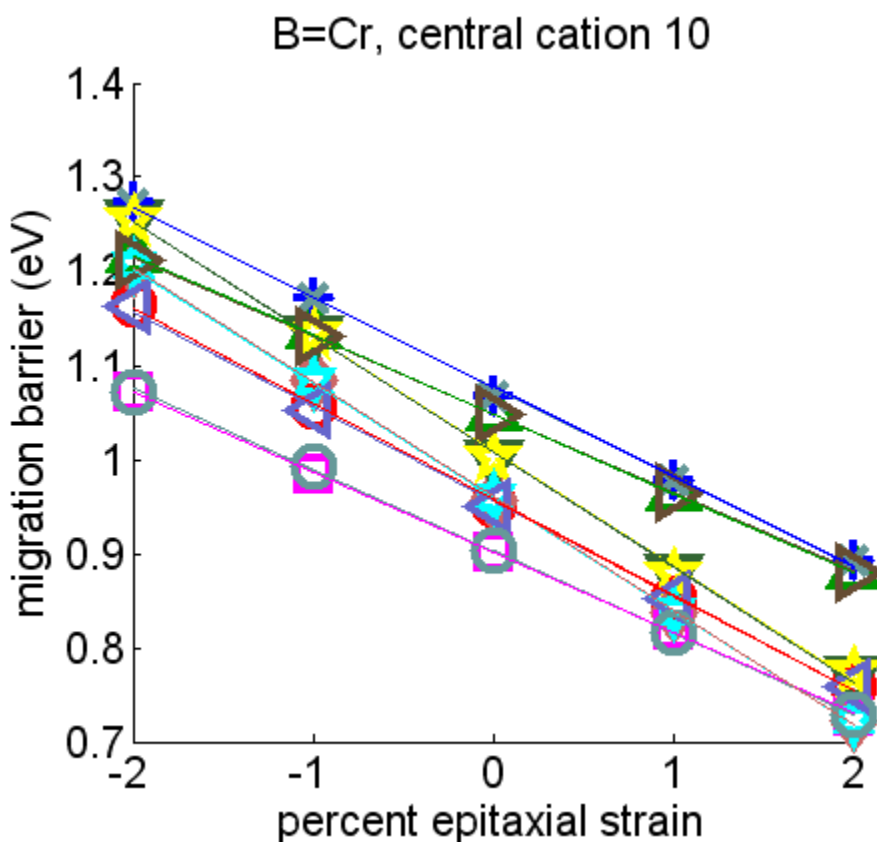


Figure S8.5. Migration barrier versus strain for LaCrO_3 , central cation position 10.

Figure S8.5. Migration barrier versus strain for LaCrO_3 with central cation position 10, for hops in the direction of initial endpoint to final endpoint, giving a representative example that all migration barriers decrease with increasing tensile strain.

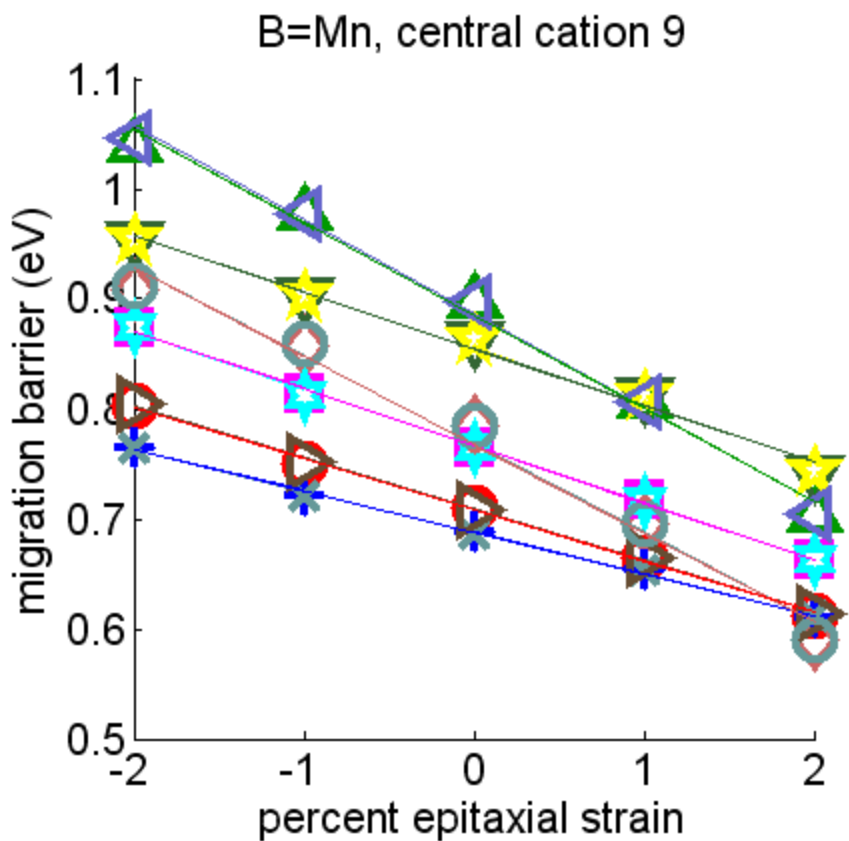


Figure S8.6. Migration barrier versus strain for LaMnO₃, central cation position 9

Figure S8.6. Migration barrier versus strain for LaMnO₃ with central cation position 9, for hops in the direction of initial endpoint to final endpoint, giving a representative example that all migration barriers decrease with increasing tensile strain.

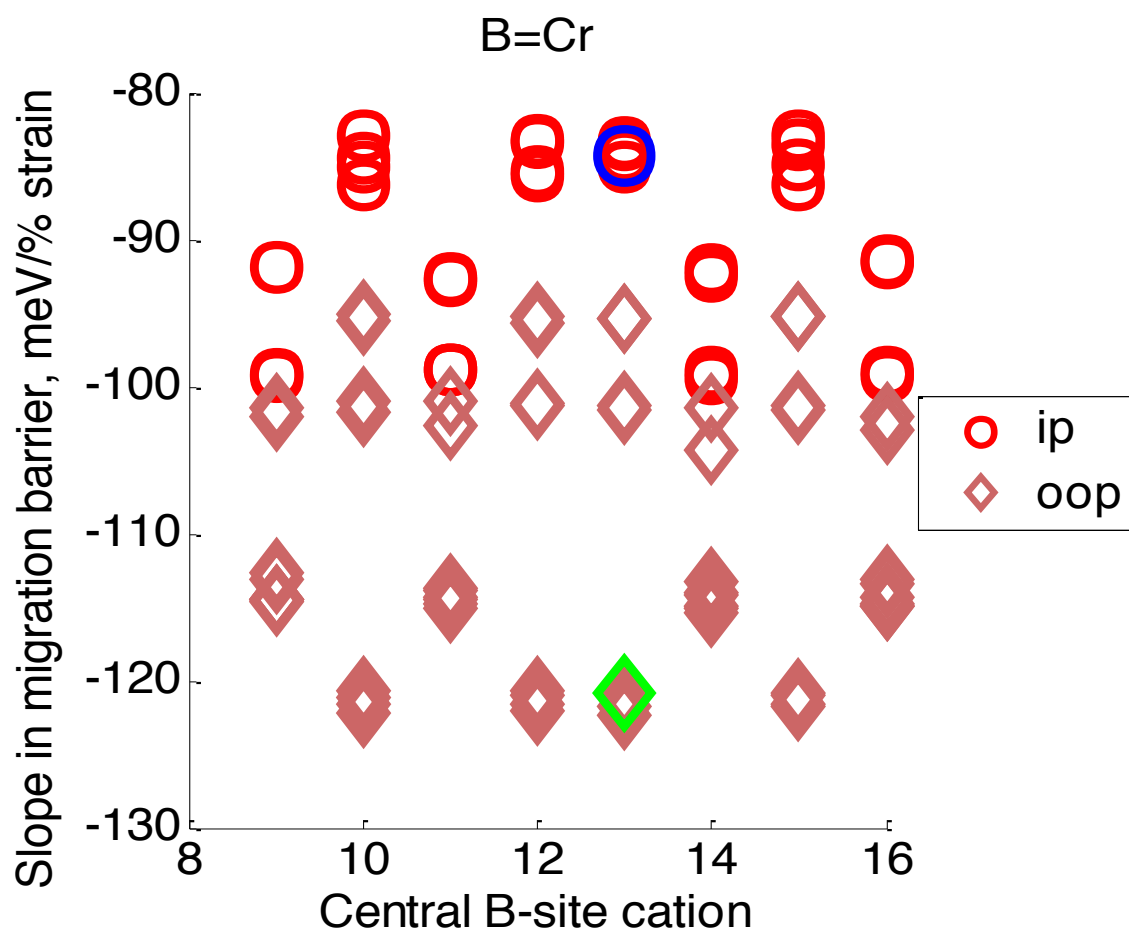


Figure S8.7. Slopes in migration barrier for LaCrO₃, all hops.

Figure S8.7. Slopes in migration barrier for LaCrO₃, all hops, in the direction of initial endpoint to final endpoint. The in-plane hop used for all systems and the out-of-plane hop used for all systems (described in Section S8) are highlighted in blue and green, respectively.

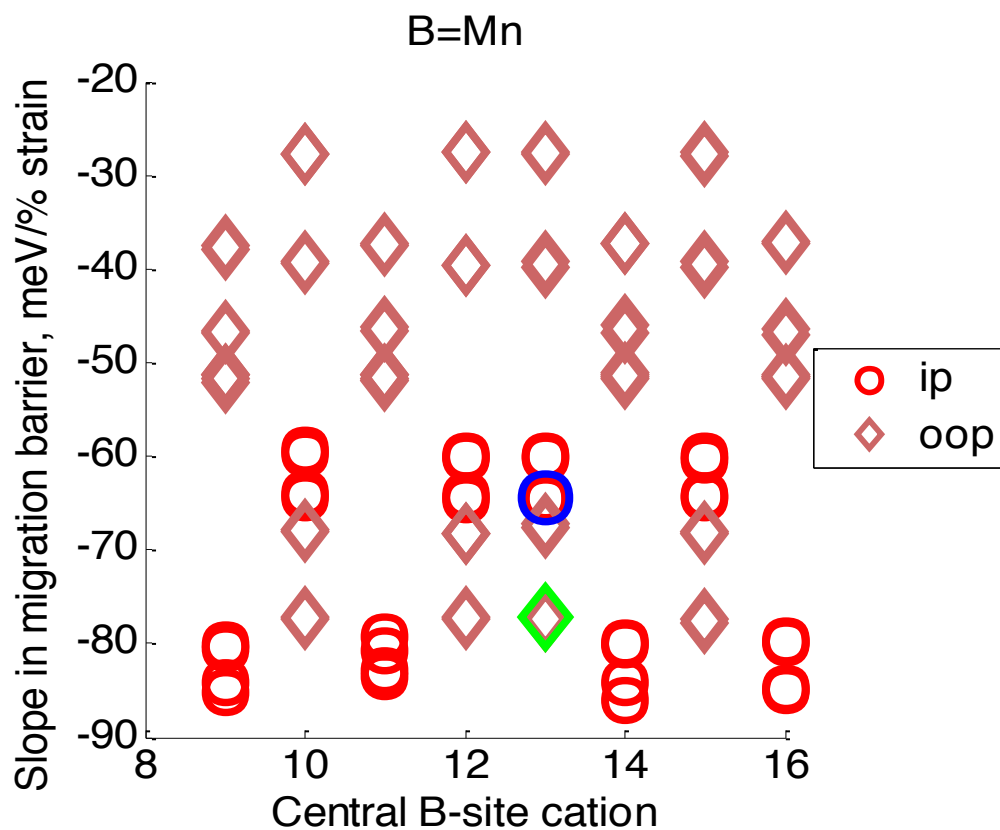


Figure S8.8. Slopes in migration barrier for LaMnO₃, all hops.

Figure S8.8. Slopes in migration barrier for LaMnO₃, all hops, in the direction of initial endpoint to final endpoint. The in-plane hop used for all systems and the out-of-plane hop used for all systems (described in Section S8) are highlighted in blue and green, respectively.

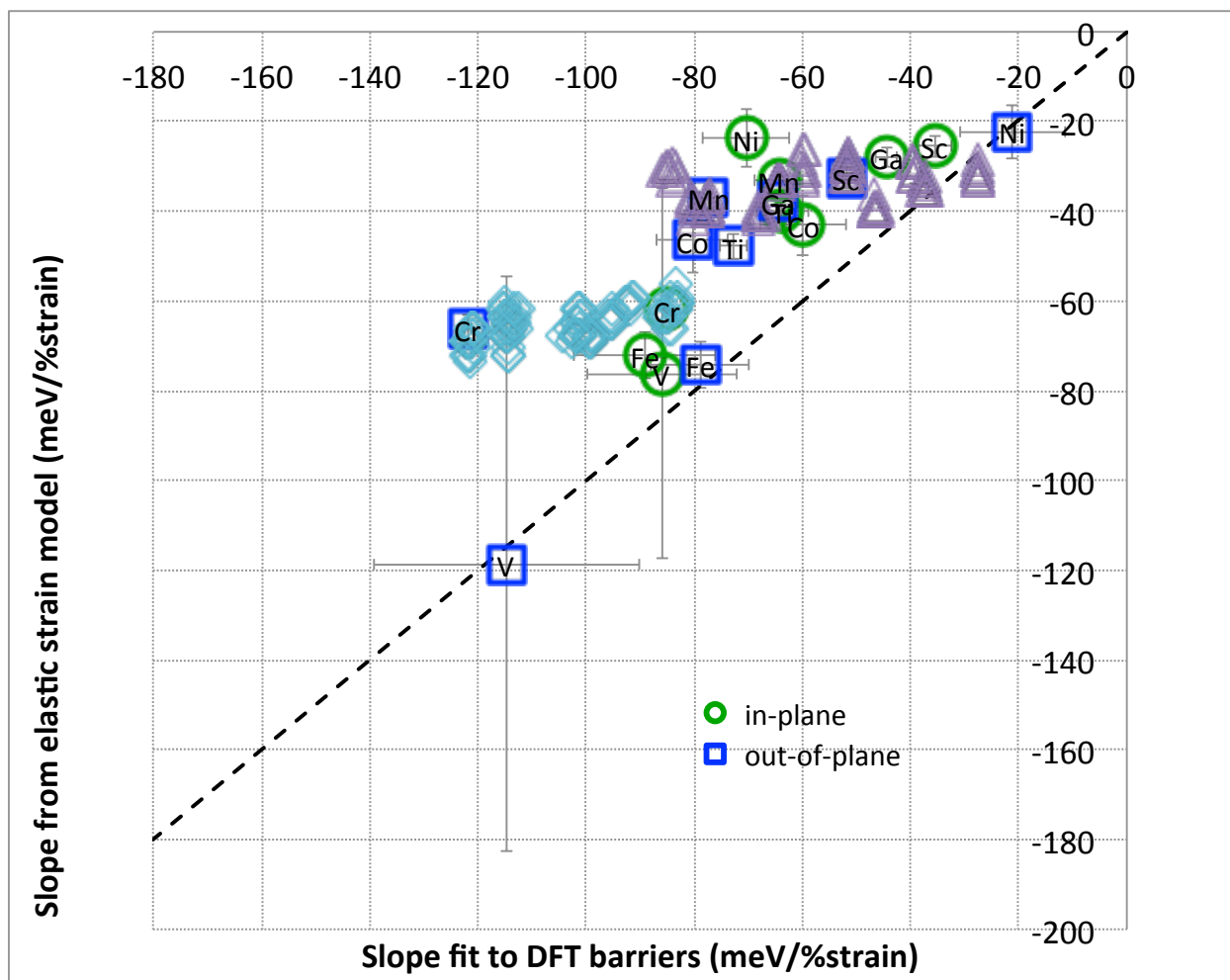


Figure S8.9. Elastic strain model slopes versus slopes fit to DFT barriers, all LaCrO₃ and LaMnO₃ hops represented

Figure S8.9. Elastic strain model slopes versus slopes fit to DFT barriers, with all LaCrO₃ and LaMnO₃ hops represented (light blue diamonds for LaCrO₃ and purple triangles for LaMnO₃). The elastic strain model slope for each hop was calculated using that particular hop's no-strain Birch-Murnaghan calculated migration volume.

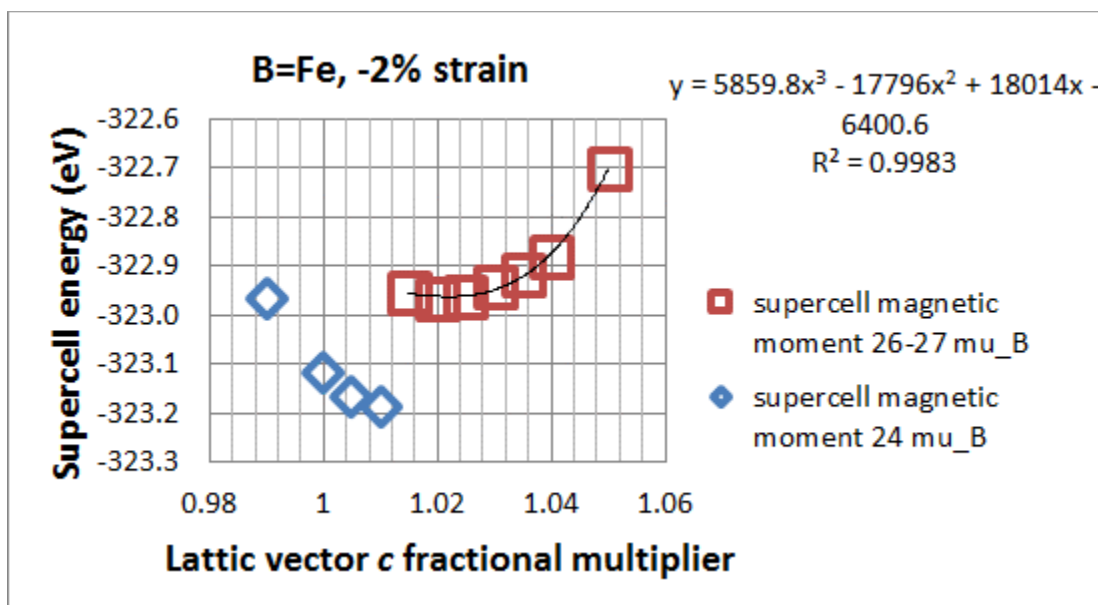


Figure S10.1. Example of cubic fitting for lattice vector *c* fractional multiplier.

Figure S10.1. Example of cubic fitting for lattice vector *c* fractional multiplier, for the B=Fe system at -2% biaxial strain. The volume-conserving multiplier would be around 1.04. The actual fit multiplier turns out to be 1.021. Note that there are two distinct magnetic moment curves.

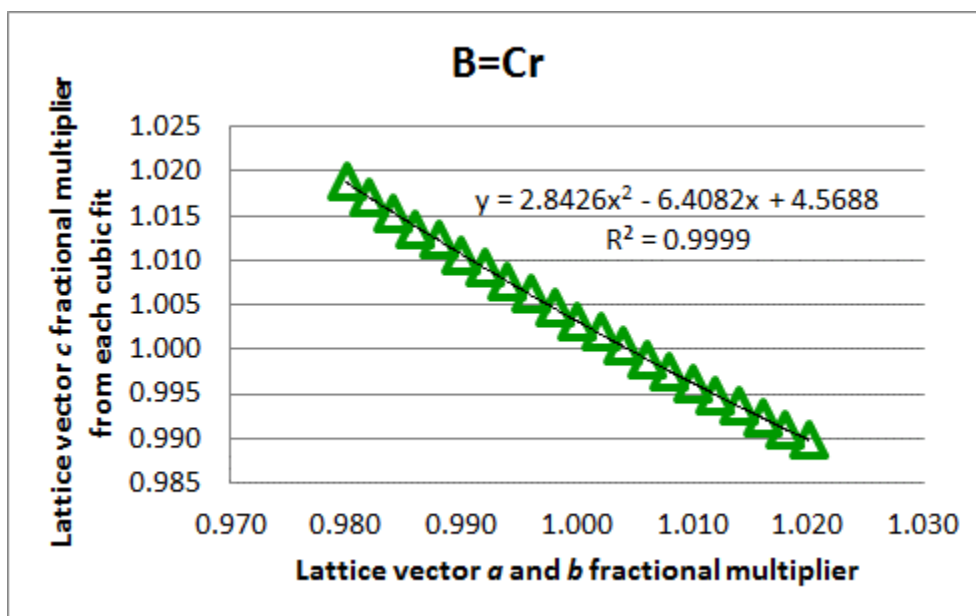


Figure S10.2. Fine-gridding for B=Cr.

Figure S10.2. Fine-gridding for the B=Cr system, showing a smooth curve. Each lattice vector *c* response multiplier was the result of a separate 7-point cubic fit at the given strain in lattice vectors *a* and *b*.

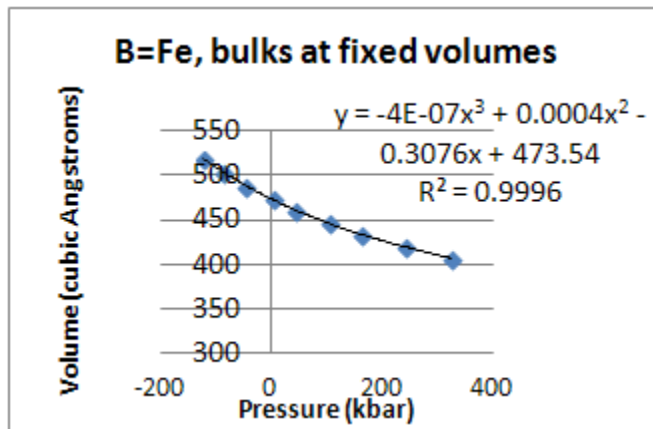


Figure S12.1. Sample V(P) curve showing a cubic fit.

Figure S12.1. Sample V(P) curve showing a cubic fit.

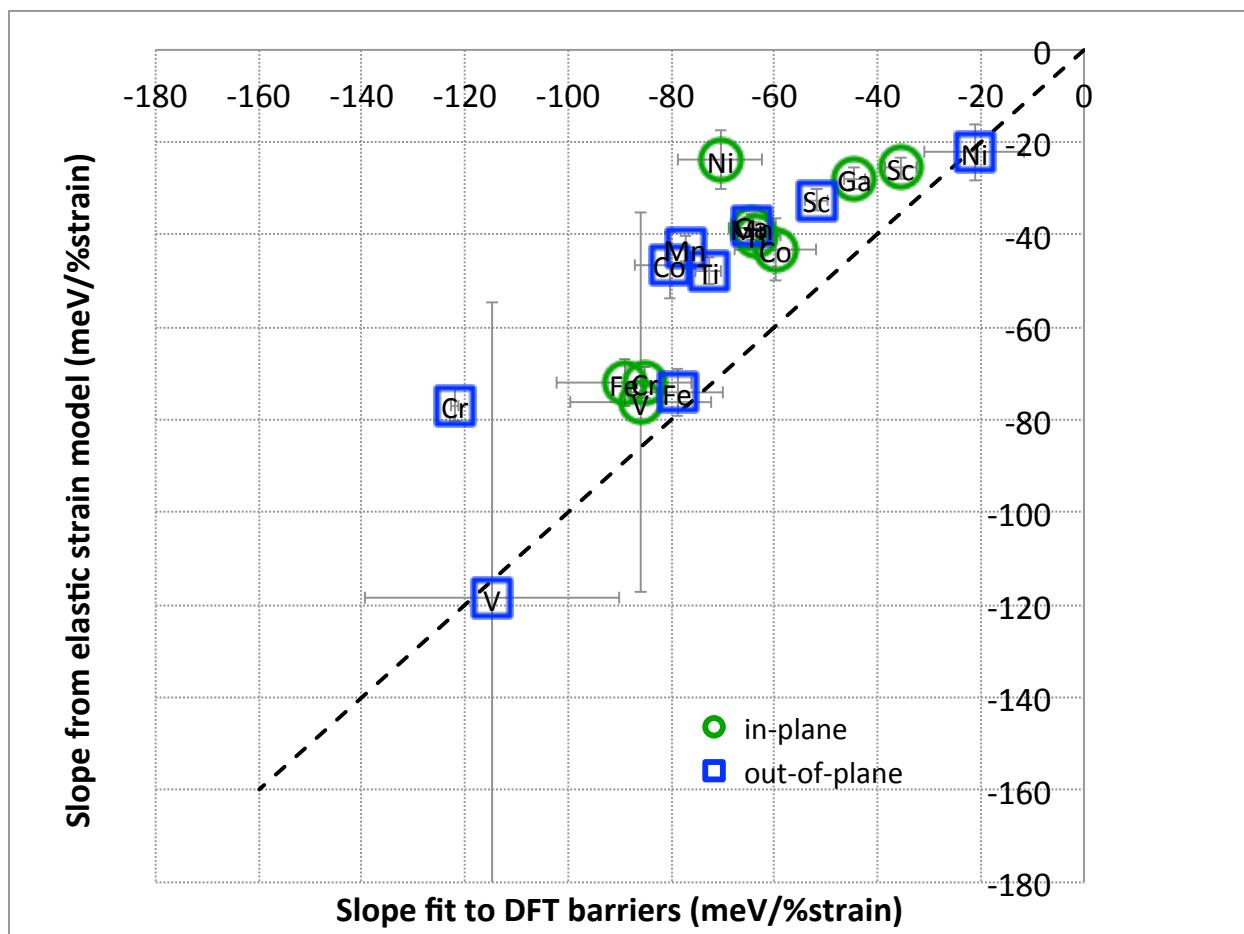


Figure S12.2. Vacancy effects on elastic model (compare with Figure 4 in main paper).

Figure S12.2. Vacancy effects on elastic model (compare with Figure 4 in main paper). The largest shift effect is shown; see points B=Cr and B=Mn.

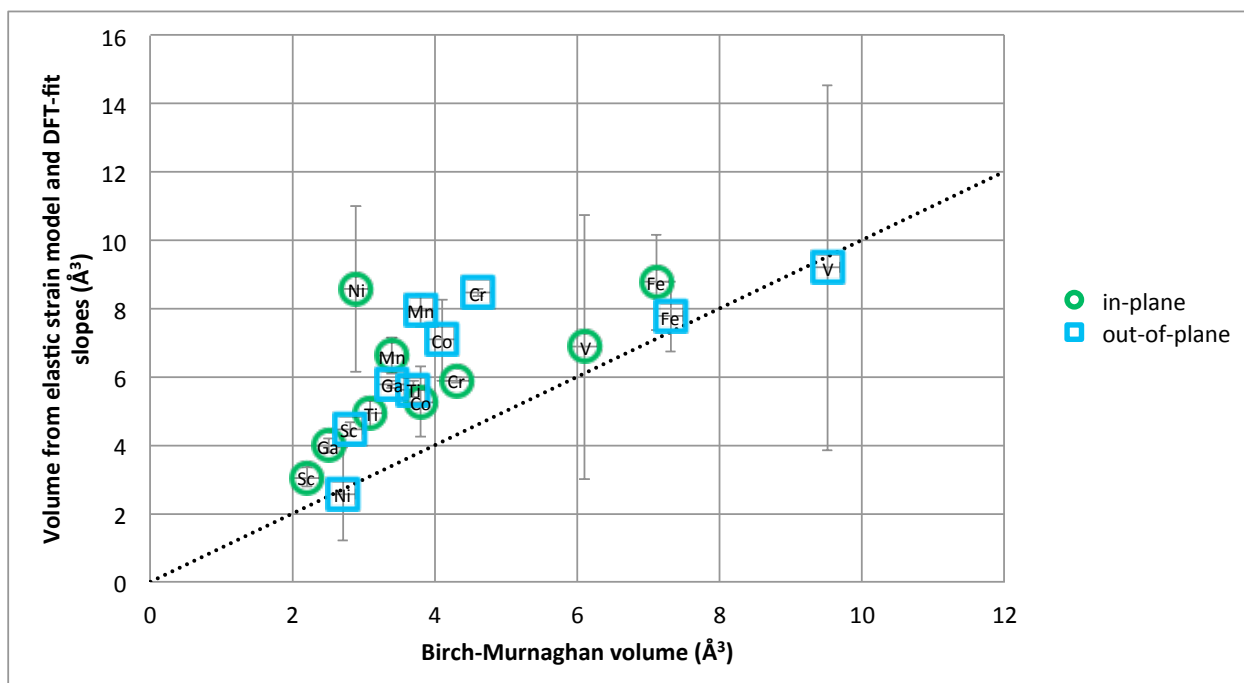


Figure S12.3. Using elastic model to try to predict V_{mig} (BM)

Figure S12.3. Elastic model migration volume versus Birch-Murnaghan formula migration volume. Data point is the center of each symbol.

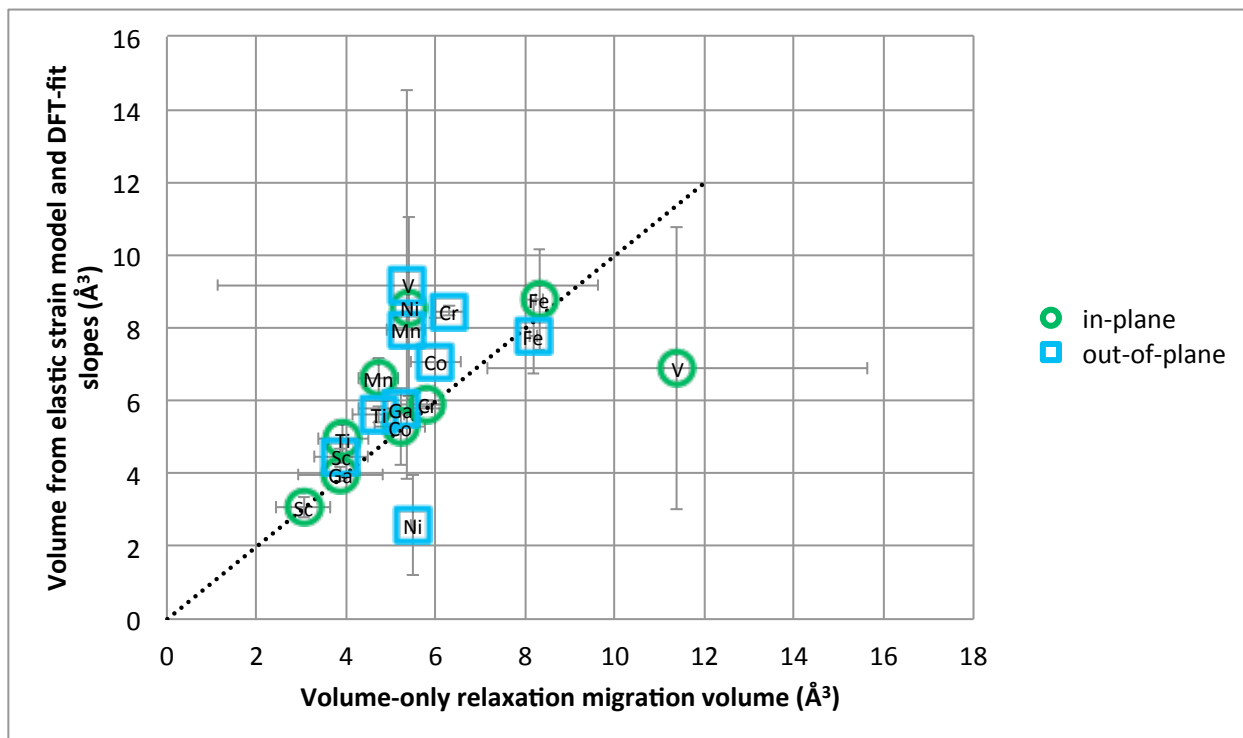


Figure S12.4. Using elastic model to try to predict Vmig (volume-only relaxation)

Figure S12.4. Elastic model migration volume versus volume-only relaxation migration volume. Data point is the center of each symbol.

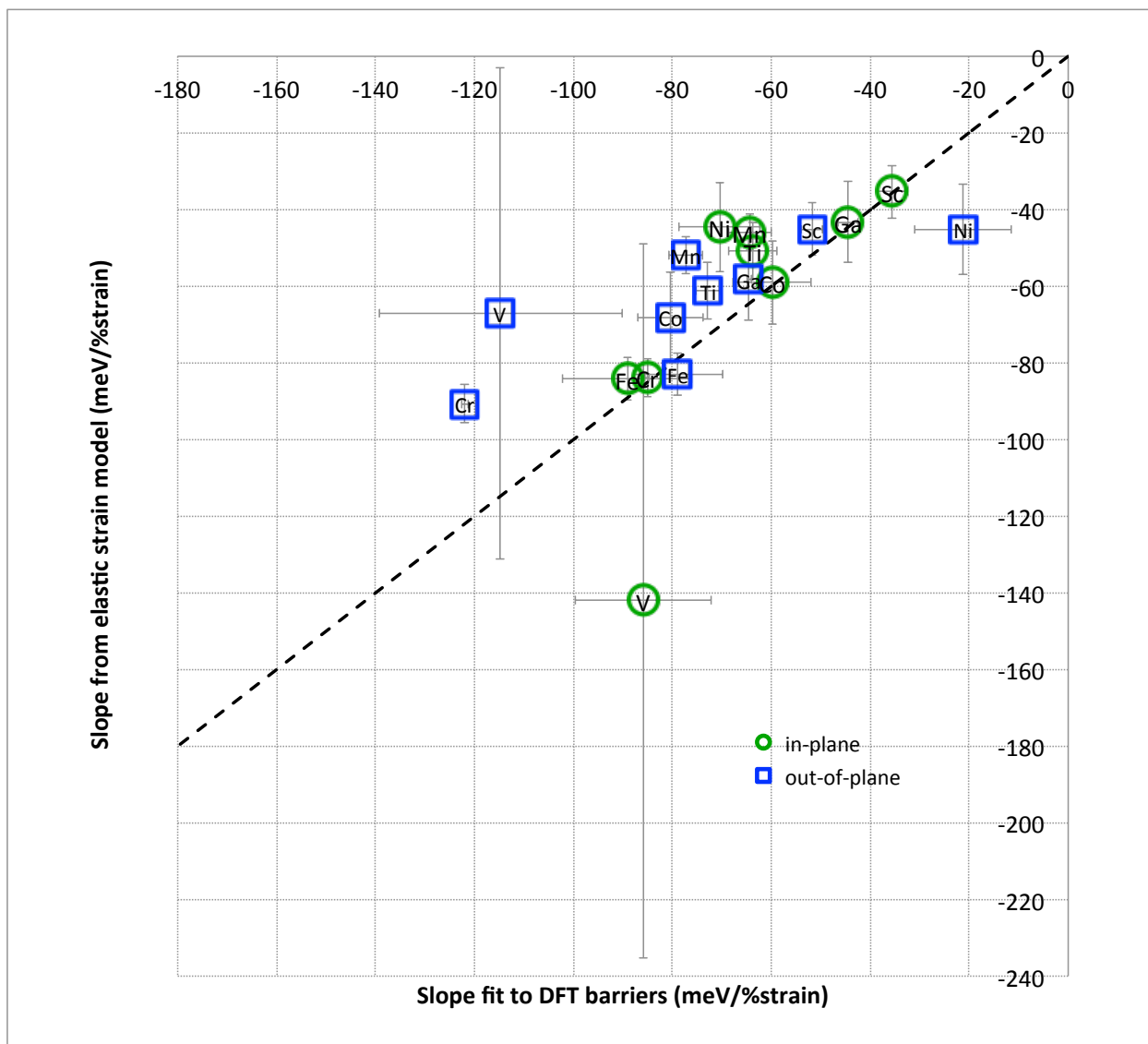


Figure S12.5. Using elastic model to try to predict slopes, with V_{mig} from volume-only relaxation

Figure S12.5. Elastic model-calculated slopes using volume-relaxation volumes, versus DFT-fit slopes. Data point is the center of each symbol.

References

1. K. Momma and F. Izumi, *Journal of Applied Crystallography*, 2008, 41, 653-658.
2. G. Kresse, Pseudopotentials (Part II) and PAW, <http://cms.mpi.univie.ac.at/vasp-workshop/slides/pseudopp2.pdf>, Accessed 2011.
3. Y.-L. Lee, J. Kleis, J. Rossmeisl and D. Morgan, *Physical Review B*, 2009, 80.
4. G. Kresse, M. Marsman and J. Furthmüller, 2011.
5. G. Henkelman, B. P. Uberuaga and H. Jónsson, *The Journal of Chemical Physics*, 2000, 113, 9901.
6. D. Sheppard, R. Terrell and G. Henkelman, *J Chem Phys*, 2008, 128, 134106.
7. Python, <https://http://www.python.org>.
8. T. Angsten, T. Mayeshiba, H. Wu and D. Morgan, *New Journal of Physics*, 2014, 16, 015018.
9. P. E. Blöchl, O. Jepsen and O. K. Andersen, *Physical Review B*, 1994, 49, 16223-16233.
10. V. I. Anisimov, F. Aryasetiawan and A. I. Lichtenstein, *Journal of Physics: Condensed Matter*, 1997, 9, 767-808.
11. J. S. Hummelshøj, D. D. Landis, J. Voss, T. Jiang, A. Tekin, N. Bork, M. Dulak, J. J. Mortensen, L. Adamska, J. Andersin, J. D. Baran, G. D. Barmparis, F. Bell, A. L. Bezanilla, J. Bjork, M. E. Bjorketun, F. Bleken, F. Buchter, M. Burke, P. D. Burton, B. B. Buus, A. Calborean, F. Calle-Vallejo, S. Casolo, B. D. Chandler, D. H. Chi, I. Czekaj, S. Datta, A. Datye, A. DeLaRiva, V. Despoja, S. Dobrin, M. Engelund, L. Ferrighi, P. Frondelius, Q. Fu, A. Fuentes, J. Furst, A. Garcia-Fuente, J. Gavnholt, R. Goeke, S. Gudmundsdottir, K. D. Hammond, H. A. Hansen, D. Hibbitts, E. Hobi, Jr., J. G. Howalt, S. L. Hrubby, A. Huth, L. Isaeva, J. Jelic, I. J. Jensen, K. A. Kacprzak, A. Kelkkanen, D. Kelsey, D. S. Kesanakurthi, J. Kleis, P. J. Klupfel, I. Konstantinov, R. Korytar, P. Koskinen, C. Krishna, E. Kunkes, A. H. Larsen, J. M. Lastra, H. Lin, O. Lopez-Acevedo, M. Mantega, J. I. Martinez, I. N. Mesa, D. J. Mowbray, J. S. Myrdal, Y. Natanzon, A. Nistor, T. Olsen, H. Park, L. S. Pedroza, V. Petzold, C. Plaisance, J. A. Rasmussen, H. Ren, M. Rizzi, A. S. Ronco, C. Rostgaard, S. Saadi, L. A. Salguero, E. J. Santos, A. L. Schoenhalz, J. Shen, M. Smedemand, O. J. Stausholm-Moller, M. Stibius, M. Strange, H. B. Su, B. Temel, A. Toftelund, V. Tripkovic, M. Vanin, V. Viswanathan, A. Vojvodic, S. Wang, J. Wellendorff, K. S. Thygesen, J. Rossmeisl, T. Bligaard, K. W. Jacobsen, J. K. Nørskov and T. Vegge, *J Chem Phys*, 2009, 131, 014101.
12. D. J. Mowbray, J. I. Martinez, F. Calle-Vallejo, J. Rossmeisl, K. S. Thygesen, K. W. Jacobsen and J. K. Nørskov, *The Journal of Physical Chemistry C*, 2011, 115, 2244-2252.
13. L. Wang, T. Maxisch and G. Ceder, *Physical Review B*, 2006, 73.
14. B. Dorado, B. Amadon, M. Freyss and M. Bertolus, *Physical Review B*, 2009, 79.
15. H. Y. Geng, Y. Chen, Y. Kaneta, M. Kinoshita and Q. Wu, *Physical Review B*, 2010, 82.
16. B. Meredig, A. Thompson, H. A. Hansen, C. Wolverton and A. van de Walle, *Physical Review B*, 2010, 82.
17. F. Zhou, M. Cococcioni, C. Marianetti, D. Morgan and G. Ceder, *Physical Review B*, 2004, 70.
18. Y. Nohara, S. Yamamoto and T. Fujiwara, *Physical Review B*, 2009, 79.
19. J. B. Goodenough, *Magnetism and the Chemical Bond*, Interscience Publishers, New York, 1963.
20. M. Cwik, T. Lorenz, J. Baier, R. Müller, G. André, F. Bourée, F. Lichtenberg, A. Freimuth, R. Schmitz, E. Müller-Hartmann and M. Braden, *Physical Review B*, 2003, 68.
21. J. B. Goodenough, *Annual Review of Materials Research*, 2003, 33, 91-128.
22. D. Lybye, F. W. Poulsen and M. Mogensen, *Solid State Ionics*, 2000, 128, 91-103.
23. P. Knauth and H. L. Tuller, *J Am Ceram Soc*, 2002, 85, 1654-1680.
24. R. A. De Souza and J. A. Kilner, *Solid State Ionics*, 1998, 106, 175-187.
25. S. Miyoshi and M. Martin, *Phys. Chem. Chem. Phys.*, 2009, 11, 3063.
26. B. Puchala, Y.-L. Lee and D. Morgan, *Journal of The Electrochemical Society*, 2013, 160, F877-F882.
27. H. Inaba and H. Tagawa, *Solid State Ionics*, 1996, 83, 1-16.
28. T. Ishigaki, S. Yamauchi, K. Kishio, J. Mizusaki and K. Fueki, *Journal of Solid State Chemistry*, 1988, 73, 179-187.
29. A. Kushima, S. Yip and B. Yildiz, *Physical Review B*, 2010, 82.
30. fuelcellmaterials.com, <http://www.fuelcellmaterials.com>.
31. T. Garnier, V. R. Manga, P. Bellon and D. R. Trinkle, *Physical Review B*, 2014, 90.
32. B. Cui, C. Song, G. Y. Wang, H. J. Mao, F. Zeng and F. Pan, *Scientific reports*, 2013, 3, 2542.
33. A. Kushima and B. Yildiz, *Journal of Materials Chemistry*, 2010, 20, 4809.

34. N. Schichtel, C. Korte, D. Hesse and J. Janek, *Physical chemistry chemical physics : PCCP*, 2009, 11, 3043-3048.
35. R. R. Hocking, in *Methods and Applications of Linear Models Regression and the Analysis of Variance, 2nd Edition* Wiley-Interscience, Hoboken, N.J., 2003, DOI: 10.1002/0471434159, pp. 28-39.
36. A. P. Boresi, K. P. Chong and J. D. Lee, *Elasticity in Engineering Mechanics, Third Edition*, Wiley-Interscience, Hoboken, N.J., 2011.
37. J. R. Barber, *Elasticity (Solid Mechanics and its Applications Volume 12)*, Kluwer Academic Publishers, Dordrecht, Netherlands, 1992.
38. W. D. Callister Jr., *Materials Science and Engineering, An Introduction*, John Wiley & Sons, Inc., New York, NY, Fifth edn., 2000.
39. E. Finazzi, C. Di Valentin, G. Pacchioni and A. Selloni, *J Chem Phys*, 2008, 129, 154113.
40. J. Kikuchi, H. Yasuoka, Y. Kokubo and Y. Ueda, *Journal of the Physical Society of Japan*, 1994, 63, 3577-3580.
41. W. C. Koehler and E. O. Wollan, *J. Phys. Chem. Solids*, 1957, 2, 100-106.
42. T. Saitoh, T. Mizokawa, A. Fujimori, M. Abbate, Y. Takeda and M. Takano, *Physical Review B*, 1997, 55, 4257-4266.
43. K. Sreedhar, J. Honig, M. Darwin, M. McElfresh, P. Shand, J. Xu, B. Crooker and J. Spalek, *Physical Review B*, 1992, 46, 6382-6386.
44. J. B. Goodenough, *Physical Review*, 1967, 164, 785-789.
45. J. P. Goral and J. E. Greedan, *Journal of Magnetism and Magnetic Materials*, 1983, 37, 315-321.
46. P. Dougier and P. Hagenmuller, *J. Solid State Chem.*, 1974, 11, 177-183.
47. N. V. Chezhina, É. V. Bodritskaya, N. a. Zhuk, V. V. Bannikov, I. R. Shein and a. L. Ivanovskii, *Physics of the Solid State*, 2008, 50, 2121-2126.
48. I. Yasuda and M. Hishinuma, *Journal of Solid State Chemistry*, 1995, 115, 152-157.
49. A. Belzner, T. Gur and R. Huggins, *Solid State Ionics*, 1992, 57, 327-337.
50. T. Ishigaki, S. Yamauchi, J. Mizusaki, K. Fueki and H. Tamura, *Journal of Solid State Chemistry*, 1984, 54, 100-107.